Check for updates

Directed evolution of adeno-associated virus for efficient gene delivery to microglia

Rui Lin [1,7] ✉, Youtong Zhou[1,2,7], Ting Yan[1,3,4,7], Ruiyu Wang[1,5,7], Heng Li[1,3,6], Zhaofa Wu [5], Xinshuang Zhang[2], Xiangyu Zhou[2], Fei Zhao[2], Li Zhang [2], Yulong Li [2,5] and Minmin Luo [1,2,6] ✉

As the resident immune cells in the central nervous system (CNS), microglia orchestrate immune responses and dynamically sculpt neural circuits in the CNS. Microglial dysfunction and mutations of microglia-specific genes have been implicated in many diseases of the CNS. Developing effective and safe vehicles for transgene delivery into microglia will facilitate the studies of microglia biology and microglia-associated disease mechanisms. Here, we report the discovery of adeno-associated virus (AAV) variants that mediate efficient in vitro and in vivo microglial transduction via directed evolution of the AAV capsid protein. These AAV-cMG and AAV-MG variants are capable of delivering various genetic payloads into microglia with high efficiency, and enable sufficient transgene expression to support fluorescent labeling, Ca^{2+} and neurotransmitter imaging and genome editing in microglia in vivo. Furthermore, single-cell RNA sequencing shows that the AAV-MG variants mediate in vivo transgene delivery without inducing microglia immune activation. These AAV variants should facilitate the use of various genetically encoded sensors and effectors in the study of microglia-related biology.

As the resident macrophages, microglia account for approximately 10% of the total cell population in the central nervous system (CNS)[1]. Originally viewed as debris scavengers, microglia are now considered the key regulator of the CNS under both normal and pathological conditions[1,2]. Microglia conduct active surveillance[3] and initiate rapid innate and adaptive immune responses upon encountering immune assaults[4,5]. Beyond their functions in immunity, microglia have multifaceted roles in controlling neural circuit development[6,7] and plasticity[8–11]. Microglial dysfunction is a key factor in CNS ageing[12] and in the progression of CNS diseases including neurodegenerative disorders[13–15] and brain cancers[16–18]. Clinical studies have identified risk-associated alterations in genes that are highly expressed in microglia[19–21], highlighting the engagement of microglia in CNS disease progression and the potential for targeting microglia for therapeutic interventions.

A key challenge in studying microglia lies in the difficulty in efficiently labeling and manipulating them. Current approaches rely on generating germline transgenic mouse models to introduce transgenes or genetic modifications into microglia, which is time-consuming, laborious, and inefficient. Recombinant viral vectors represent an attractive alternative for manipulating microglia. In particular, owing to the low pathogenicity, recombinant adeno-associated viruses (rAAVs) are now the most frequently used viral vectors in basic research and in gene therapies[22–24]. Despite their ability to transduce a wide range of cell types in mammals, rAAVs packaged using existing AAV capsids have not achieved a high transduction rate and a sufficient transgene expression level in microglia, especially in vivo[25–30]. Viral transduction of microglia (and macrophages in general) also faces the potential issue of inducing immune activation[26,31]. To overcome these major technical challenges, we conducted directed evolution to develop AAV vectors with engineered capsids that enable efficient gene delivery to microglia.

Results

Identifying AAV-cMGs for in vitro microglial transduction. Using the wild-type AAV9 capsid as a starting point, we generated a capsid library in which each variant harbors a random seven-amino-acid insertion between amino acids 588 and 589 of the AAV9 VP1 protein (Fig. 1). This insertion site is located at the protrusions of the capsid's threefold symmetry axis, which facilitates the interactions between inserted peptides and membrane molecules on target cells[32–34]. We transduced cultured mouse microglia with the capsid library rAAVs and recovered those capsid variants that successfully mediated transduction. Then, we packaged recovered capsid variants into rAAVs and screened them again in cultured mouse microglia (Fig. 1a). Using next-generation sequencing, we identified capsid variants that were highly enriched after two rounds of screening (Fig. 1b and Supplementary Table 1). We packaged a single-stranded mScarlet reporter vector into rAAVs using candidate capsid variants and transduced cultured mouse microglia with the individual rAAV variants. We evaluated their transduction abilities against the parental AAV9, as well as against AAV5 and AAV8 and against AAV6 with a Y731F/Y705F/T492V triple mutation (AAV6TM) that has been reported to transduce cultured mouse microglia[26].

Two capsid variants showed superior transduction of cultured microglia among all candidates tested. The first variant harbors a WPPKTTS heptamer insertion (hereafter referred to as AAV-cMG.WPP; Fig. 1b). The second variant harbors a QRPPREP heptamer insertion (hereafter referred to as AAV-cMG.QRP; Fig. 1b). Both AAV-cMG.QRP (~55%) and AAV-cMG.WPP (~75%) achieved substantially higher transduction rates compared with the AAV5 (~12%), AAV6TM (~3%), AAV8 (~34%) or AAV9 (~10%) capsids (Fig. 1e,g). AAV-cMG.WPP also drove stronger mScarlet expression than did the AAV5, AAV6TM, AAV8 or AAV9 capsids (Fig. 1g).

[1]National Institute of Biological Sciences (NIBS), Beijing, China. [2]Chinese Institute for Brain Research, Beijing, China. [3]School of Life Sciences, Tsinghua University, Beijing, China. [4]Tsinghua-Peking Center for Life Sciences, Tsinghua University, Beijing, China. [5]School of Life Sciences, Peking University, Beijing, China. [6]Tsinghua Institute of Multidisciplinary Biomedical Research (TIMBR), Beijing, China. [7]These authors contributed equally: Rui Lin, Youtong Zhou, Ting Yan, Ruiyu Wang. ✉e-mail: linrui@nibs.ac.cn; luominmin@nibs.ac.cn
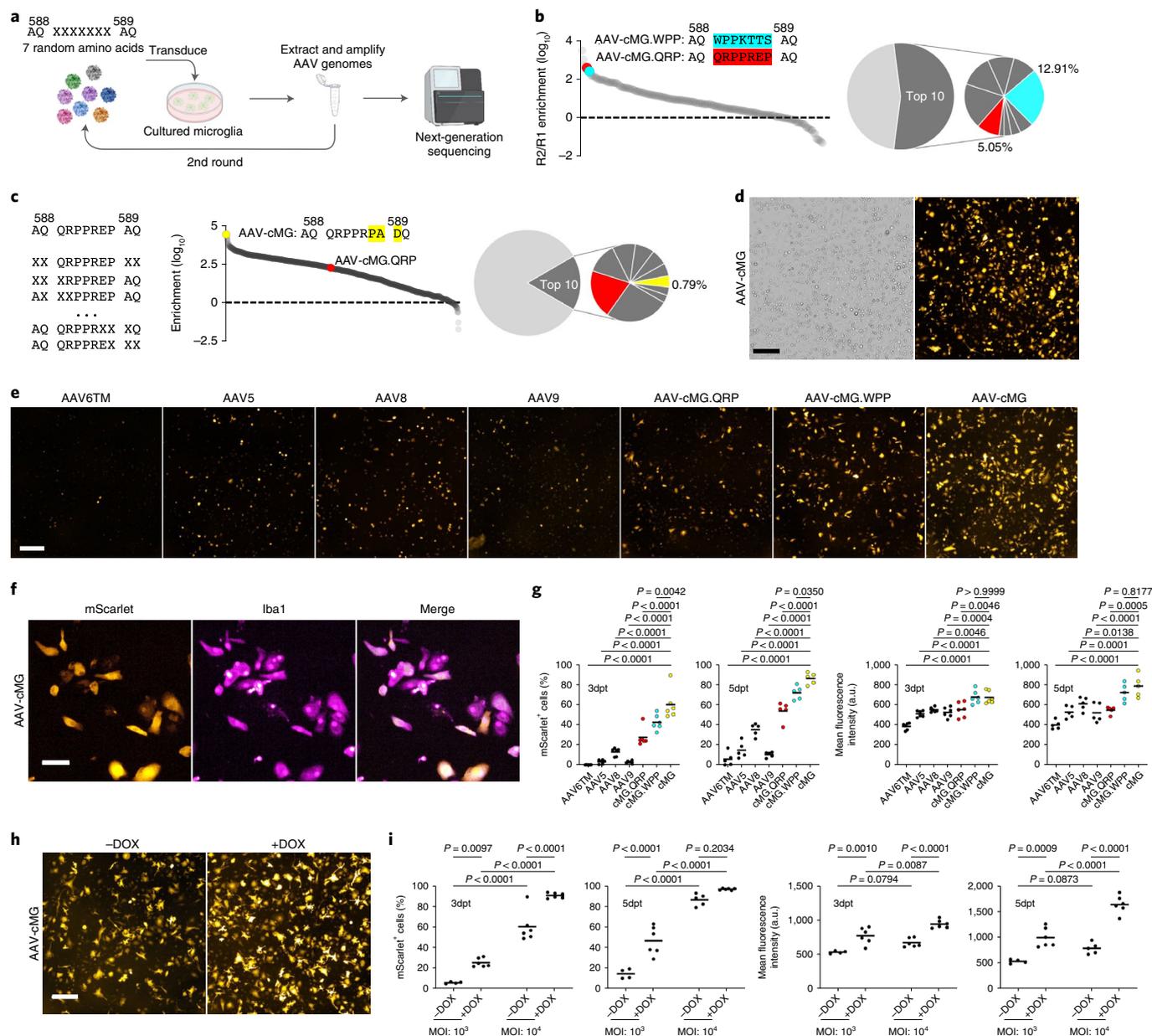
Fig. 1 | AAV-cMG mediates efficient gene transduction in cultured microglia. a, Schematic diagram of the selection process. Seven random amino acids were inserted between the amino acids at positions 588 and 589 of the AAV9 VP1 protein. The library was screened in cultured mouse microglia for two rounds. **b**, Distribution of AAV9 capsid variants recovered from cultured mouse microglia, sorted by decreasing order of enrichment score. The pie chart shows the normalized frequency of AAV-cMG.QRP (red) and AAV-cMG.WPP (cyan) in the total recovered sequences. **c**, Schematic diagram of the selection process of AAV-cMG.QRP variants. The right panel shows the distribution of AAV-cMG.QRP variants recovered from cultured mouse microglia, sorted by decreasing order of enrichment score. The pie chart shows the normalized frequency of AAV-cMG (yellow) and AAV-cMG.QRP (red) in the total recovered sequences. **d**, Representative images of cultured mouse microglia transduced with mScarlet reporter AAVs packaged using AAV-cMG. Scale bar, 200 μm. **e**, Representative images of cultured mouse microglia transduced with mScarlet reporter AAVs packaged using different capsids. Scale bar, 200 μm. **f**, Representative immunofluorescence images showing the colocalization of mScarlet- and Iba-positive immunosignals in cultured mouse microglia transduced with AAV-cMG-SFFV-mScarlet. Scale bar, 50 μm. **g**, Quantification of percentage of mScarlet^{+} cells and the mean fluorescence intensity of cultured mouse microglia transduced with mScarlet reporter AAVs packaged using different capsids ($n = 6$ replicates for quantification 3 days post-transduction (dpt); 5 replicates for quantification 5 dpt; one-way ANOVA with Dunnett's post-hoc test; P values as listed in the figure). Data are given as scatter and mean. **h**, Representative images showing the cultured microglia transduced by AAV-cMG-SFFV-mScarlet with or without doxorubicin (DOX). Scale bar, 200 μm. **i**, Quantification of percentage of mScarlet^{+} cells and the mean fluorescence intensity of cultured mouse microglia transduced by AAV-cMG-SFFV-mScarlet at two different levels of multiplicity of infection (MOI) with or without DOX ($n = 6$ replicates for each group except for the MOI: 10^3 –DOX group ($n = 4$) and the MOI: 10^4 +DOX 5 dpt group ($n = 5$); one-way ANOVA with Dunnett's post-hoc test; P values as listed in the figure). Data are given as scatter and mean.

To obtain variants that mediate even higher in vitro microglial transduction, we conducted further evolution of AAV-cMG.QRP. We generated another capsid library by semi-randomly mutating the inserted heptamer and the adjacent four amino acids in AAV-cMG.QRP (Fig. 1c). We screened this library again in cultured mouse microglia. One AAV-cMG.QRP variant that contains the amino acid sequence 'PAD' at positions 594–596 (hereafter referred to as AAV-cMG) was highly enriched after one round of screening (Fig. 1c and Supplementary Table 1). AAV-cMG (~86%) achieved a significantly higher transduction rate than the AAV-cMG.WPP or the parental AAV-cMG.QRP capsid (Fig. 1e–g; P values are listed in the figure; one-way ANOVA with Dunnett's post-hoc test).

To examine whether AAV-cMG-mediated transduction triggers phenotypic changes in microglia[35], we performed principal component analysis of transcriptome data from four different samples of cultured mouse microglia: control untransduced, endotoxin lipopolysaccharide (LPS)-treated, interleukin-4 (IL-4)-treated[36], and AAV-cMG-transduced. AAV-cMG-transduced microglia clustered towards control untransduced microglia, and away from LPS-treated or IL-4-treated microglia (Extended Data Fig. 1a). Differential gene expression analysis also indicated that AAV-cMG transduction did not induce proinflammatory pathways in cultured microglia (Extended Data Fig. 1b). We further analyzed transcriptome data from AAV-cMG-transduced cultured mouse microglia treated with LPS or IL-4. Both LPS and IL-4 induced strong transcriptomic signatures in AAV-cMG-transduced microglia, similar to those observed in untransduced microglia (Extended Data Fig. 1c,d), suggesting that AAV-cMG transduction does not blunt microglial responses to external stimuli.

Inhibition of topoisomerases or proteasomes facilitates rAAV transduction, both in vitro and in vivo[37–39]. We therefore examined whether doxorubicin (DOX)[40], an FDA-approved topoisomerase inhibitor, might further enhance the in vitro microglial transduction efficiency of AAV-cMG. We transduced cultured mouse microglia using AAV-cMG together with DOX (Fig. 1h). The application of DOX significantly accelerated and enhanced the transgene expression driven by AAV-cMG at two different levels of multiplicity of infection (Fig. 1h,i; P values are listed in the figure; one-way ANOVA with Dunnett's post-hoc test).

Selection of AAV-MGs for in vivo microglial transduction. Next, we attempted to identify AAV variants that could efficiently transduce microglia in vivo. To drive microglia-specific transgene expression, we utilized the Cre/loxP system. We packaged a single-stranded, Cre-dependent mScarlet reporter vector into either AAV-cMG.QRP or AAV-cMG.WPP, and injected the rAAVs into the brains of $Cx3cr1^{CreER}$ transgenic mice, which selectively express the tamoxifen-inducible Cre recombinase in microglia[8]. Although

both AAV-cMG.QRP and AAV-cMG.WPP show higher efficiency than the wild type, only a small proportion of microglia were labeled 2 weeks after virus injection (Extended Data Fig. 2). These results prompted us to further evolve AAV-cMGs for in vivo applications. We generated an AAV-cMG.WPP variants library by semi-randomly mutating the inserted heptamer and the adjacent four amino acids (Fig. 2a). We screened this library in vivo by injecting the library rAAVs into the brains of $Cx3cr1^{CreER}$ mice. We adopted the Cre recombination-based AAV targeted evolution strategy[41] to selectively recover capsid variants from Cre-recombined AAV genomes (Extended Data Fig. 3). After two rounds of screening we identified two highly enriched capsid variants (Fig. 2b and Supplementary Table 1). The first variant has the amino acid sequence 'LMT' at positions 587–589 (Fig. 2b). The second variant has the amino acid sequence 'ATE' at positions 587–589 (Fig. 2b). We named these two AAV-cMG.WPP capsid variants AAV-MG1.1 and AAV-MG1.2, respectively, and conducted detailed examination of their abilities to transduce microglia in vivo.

We used AAV-MG1.1 and AAV-MG1.2 to package a single-stranded Cre-dependent mScarlet reporter vector into rAAVs. We again injected these rAAVs into the brains of $Cx3cr1^{CreER}$ mice. Both AAV-MGs drove strong and widespread mScarlet expression in all brain areas tested (Fig. 2c and Extended Data Figs. 2,4). The in vivo microglial transduction efficiency of both AAV-MGs is higher than that of the parental AAV-cMG.WPP capsid (Fig. 2c,d and Extended Data Figs. 2,4a,b,d,e) as well as that of the AAV9, AAV6TM and AAV8 capsids (Fig. 2c and Extended Data Fig. 2). Using the immunoreactivity of ionized calcium binding adapter molecule 1 (Iba1) as a marker for microglia, we found that >80% of microglia in the core regions of the injection sites were labeled (Fig. 2e and Extended Data Fig. 4c). The mScarlet expression driven by AAV-MGs was Cre dependent (Extended Data Fig. 5a) and was restricted to microglia (Fig. 2f,g and Extended Data Fig. 5b). To further examine the specificity of Cre-dependent transgene expression by AAV-MGs, we also injected AAV-MG1.1- or AAV-MG-1.2-SFFV-DIO-mScarlet into the striatum of $Tmem119^{CreER}$ mice[42] and confirmed that both AAV-MGs drive selective mScarlet expression in microglia (Extended Data Fig. 5c,d).

The enhanced in vivo transduction of microglia by AAV-MGs was unlikely to be due to their biased transduction abilities towards microglia over other cell types in the brain, given that the AAV-MG1.1- or AAV-MG-1.2-SFFV-DIO-mScarlet also drove strong mScarlet expression in neurons and astrocytes when co-injected with an rAAV that non-selectively expresses Cre recombinase in the brains of wild-type mice (Extended Data Fig. 6a,b). Neither AAV-MG1.1 nor AAV-MG1.2 could effectively transduce cultured mouse microglia (Extended Data Fig. 6c). Also, for both AAV-MGs, DOX significantly enhanced the mScarlet

Fig. 2 | Directed evolution generates AAV-MGs that mediate efficient gene transduction in microglia in vivo. a, Schematic diagram of the in vivo selection process. Semi-random mutations were introduced into the inserted heptamer and the adjacent four amino acids in AAV-cMG.WPP. The library was screened in the striatum and the midbrain of $Cx3cr1^{CreER}$ mice. Capsid variants from Cre-recombined AAV genomes were selectively recovered from the brains using the Cre recombination-based AAV targeted evolution (CREATE) strategy. The arrows indicate the primers for amplifying heptamer insertions (yellow) from Cre-recombined AAV genomes. pA, polyadenylation signal sequence. **b**, Distribution of AAV-cMG.WPP variants recovered from the $Cx3cr1^{CreER}$ mouse brains, sorted by decreasing order of enrichment score. The pie chart shows the normalized frequency of AAV-MG1.1 (magenta) and AAV-MG1.2 (green) in the total recovered sequences. **c**, Representative images of the mScarlet expression patterns in the striatum of $Cx3cr1^{CreER}$ mice injected with AAV6TM-, AAV9-, AAV-cMG.WPP-, AAV-MG1.1-, or AAV-MG1.2-SFFV-DIO-mScarlet. Scale bar, 250 μm. **d**, Cell counts of mScarlet and Iba double-positive cells in the striatum of $Cx3cr1^{CreER}$ mice injected with AAV-cMG.WPP- ($n = 3$), AAV-MG1.1- ($n = 5$) or AAV-MG1.2-SFFV-DIO-mScarlet ($n = 5$) (two-way ANOVA with Tukey's post-hoc test; cMG.WPP versus MG1.1: $P < 0.0001$; AAV-cMG.WPP versus AAV-MG1.2: $P < 0.0001$). Data are given as mean ± s.e.m. **e**, Percentage of Iba-positive microglia that are labeled by mScarlet in the striatum of $Cx3cr1^{CreER}$ mice injected with AAV-MG1.1- or AAV-MG1.2-SFFV-DIO-mScarlet ($n = 5$ mice for each group). Quantification was conducted over an area of $1 \times 1 \, mm^2$. Data are given as mean ± s.e.m. **f**, Representative images of the colocalization of mScarlet- and Iba-positive immunosignals in the striatum of $Cx3cr1^{CreER}$ mice injected with AAV-MG1.1- or AAV-MG1.2-SFFV-DIO-mScarlet. Scale bar, 50 μm. **g**, Percentage of mScarlet-positive microglia that are labeled by Iba out of the total number of mScarlet-positive cells in the orbitofrontal cortex (OFC), the striatum, the midbrain, the thalamus and the hippocampus of $Cx3cr1^{CreER}$ mice injected with AAV-MG1.1- or AAV-MG1.2-SFFV-DIO-mScarlet ($n = 5$ mice for each group). Data are given as scatter and mean.

expression level in microglia but did not increase the number of mScarlet-labeled microglia (Fig. 2d, Extended Data Fig. 4b,e and Supplementary Fig. 1; $P < 0.0001$; two-sided unpaired Mann–Whitney test).

AAV-MGs transduction does not change microglia transcriptomes. We examined whether AAV-MGs-mediated transduction would trigger phenotypic changes in microglia in the brain

(Fig. 3a). Two weeks after the injection of the AAV-MG1.1- or AAV-MG1.2-SFFV-DIO-mScarlet into the striatum of $Cx3cr1^{CreER}$ mice, we performed single-cell RNA sequencing (scRNA-seq) of both mScarlet[+] (AAV-MGs-transduced) and mScarlet[-] (untransduced) microglia from the same mice using a modified Smart-seq2 protocol[43] (Extended Data Fig. 7a–c). We also sequenced microglia from LPS-treated mice as the control group. Visualization of the Smart-seq2 datasets using uniform manifold approximation


Fig. 3 (labels a–g)
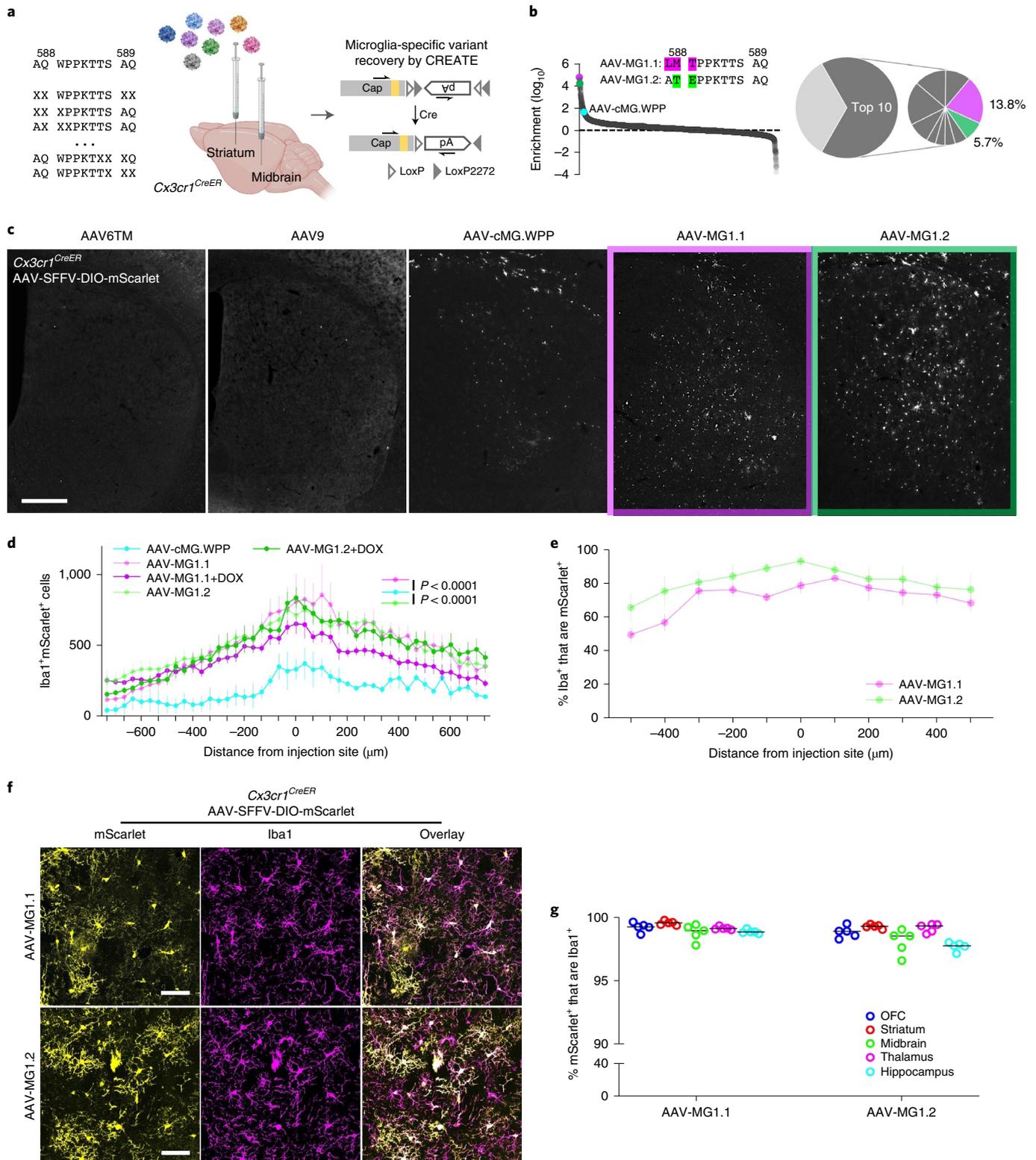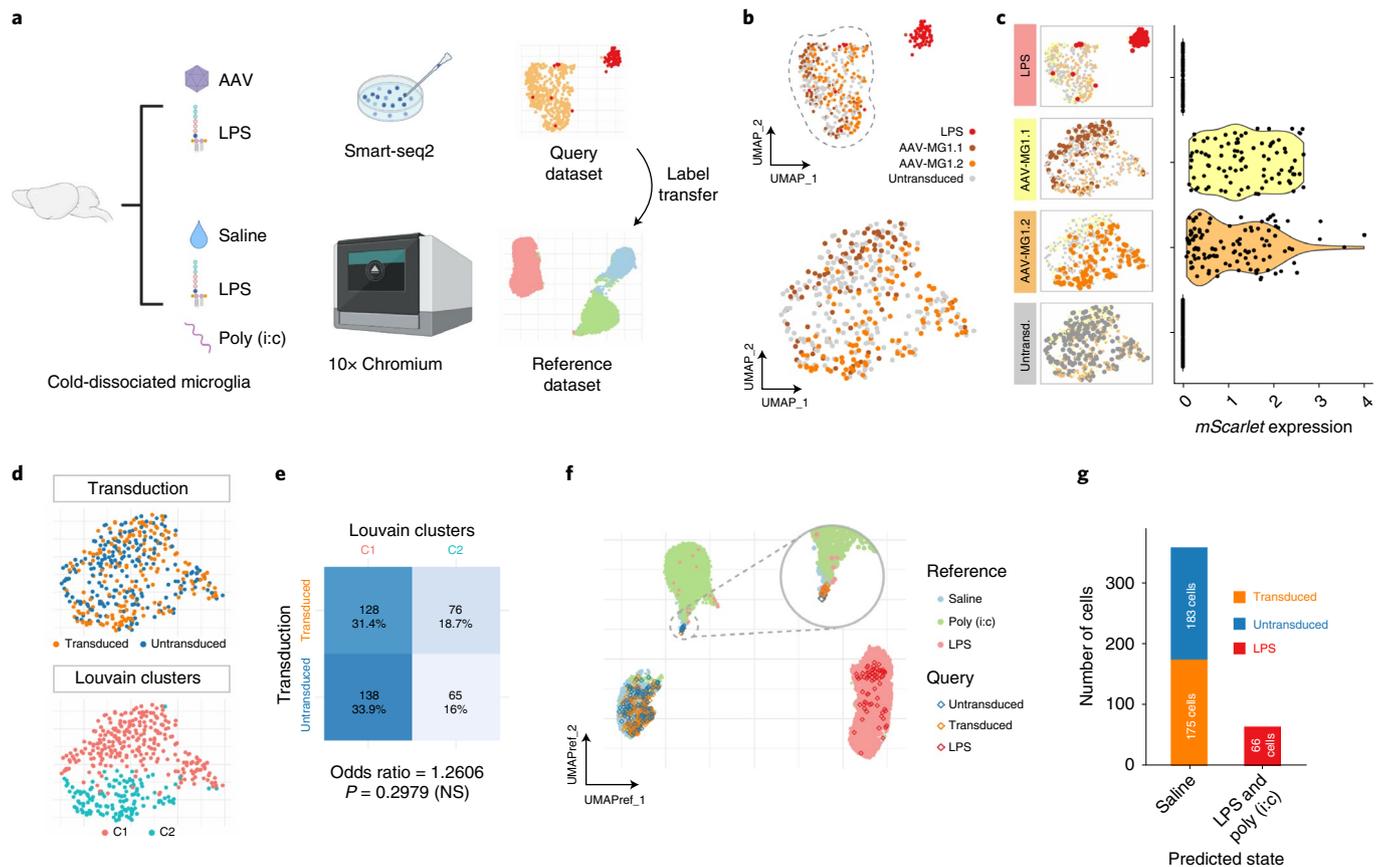
Fig. 3 | In vivo transduction of microglia by AAV-MGs does not induce microglia activation. a, Schematic diagram of the label transfer strategy to examine the transcriptional states of AAV-MGs-transduced microglia. **b**, UMAP plot of 488 microglia (90 AAV-MG1.1-transduced microglia, 114 AAV-MG1.2-transduced microglia, 203 untransduced microglia isolated from AAV-MGs-injected mice, 81 microglia isolated from LPS-treated mice) sequenced using the Smart-seq2 protocol. The bottom panel shows the rotated zoom-in view of the marked cluster in the upper panel. **c**, Violin plot showing the log-normalized expression level of the *mScarlet* transcript. **d**, UMAP plots showing the transduction states and the Louvain clusters. **e**, Contingency table used for calculating the odds ratio of AAV-MGs-transduced cells being classified in cluster 2 (C2) (chi-squared test; *P* value as given in the figure). **f**, De novo, re-computed UMAP plot of the reference microglia datasets (4,733 microglia from saline-treated mice, 8,955 microglia from LPS-treated mice and 6,758 microglia from Poly(i:c)-treated mice; sequenced using the 10x Genomics platform) and the query dataset (sequenced using the Smart-seq2 protocol). **g**, Summary of the states of the Smart-seq2 sequenced microglia, as predicted by the Seurat label transfer shown in **f**.

and projection (UMAP)[44] indicated that the untransduced and AAV-MGs-transduced microglia formed a homogeneous cluster and were well-separated from the microglia of LPS-treated mice (Fig. 3b,c). Furthermore, we performed unsupervised clustering analysis on the untransduced and AAV-MGs-transduced microglia using the Louvain clustering algorithm[45] and discovered two clusters (Fig. 3d). The odds ratio of the AAV-MGs-transduced microglia being classified in cluster 2 is close to 1 (Fig. 3e), suggesting that the transcriptional states are independent from the transduction states.

Moreover, we did not detect any substantial differences when we compared the expression of homeostatic or reactive microglia marker genes between the untransduced and AAV-MGs-transduced microglia (Extended Data Figs. 7f and 8a,b). In the AAV-MGs-transduced microglia, the expression levels of homeostatic or reactive microglia marker genes are not correlated with the expression level of *mScarlet* (Extended Data Fig. 8c,d). We also performed SCENIC ('single-cell regulatory network inference and clustering')[46] analysis on the regulon associated with *Cebpb*, a critical transcription factor for microglial activation[47] (Supplementary Fig. 2a). The analysis predicted upregulated activity of the *Cebpb* regulon in microglia from LPS-treated mice but not in the untransduced or the AAV-MGs-transduced microglia (Supplementary Fig. 2b,c). These results suggest that the transcriptional states of

microglia are not substantially affected by AAV-MGs-mediated transgene expression.

To further validate the physiological states of microglia in our Smart-seq2 datasets, we leveraged a label transfer strategy implemented in Seurat[48] to project microglia from the Smart-seq2 datasets onto the reference 10× datasets of saline-, LPS-, and polyinosinic–polycytidylic acid (Poly(i:c))-treated microglia (Fig. 3a, Extended Data Fig. 7c,d,e and Supplementary Fig. 2d,e), and re-computed a merged UMAP projection to represent the microglia states from both datasets (Fig. 3f). LPS-treated microglia in the Smart-seq2 datasets were positioned in the LPS-treated or Poly(i:c)-treated microglia cluster (Fig. 3f,g). In contrast, all untransduced and AAV-MGs-transduced microglia in the Smart-seq2 dataset were positioned in the saline-treated microglia cluster (Fig. 3f,g). Thus, these results support the notion that the transduction mediated by AAV-MGs does not induce microglia activation in vivo.

AAV-MGs enable in vivo Ca²⁺ and ATP imaging in microglia. We next tested whether AAV-MGs can deliver various genetic payloads into microglia for functional studies. We expressed two genetically encoded fluorescent sensors in microglia to examine the physiological responses of microglia towards peripheral endotoxin challenge (Fig. 4a). We first used AAV-MG1.2 to package a single-stranded
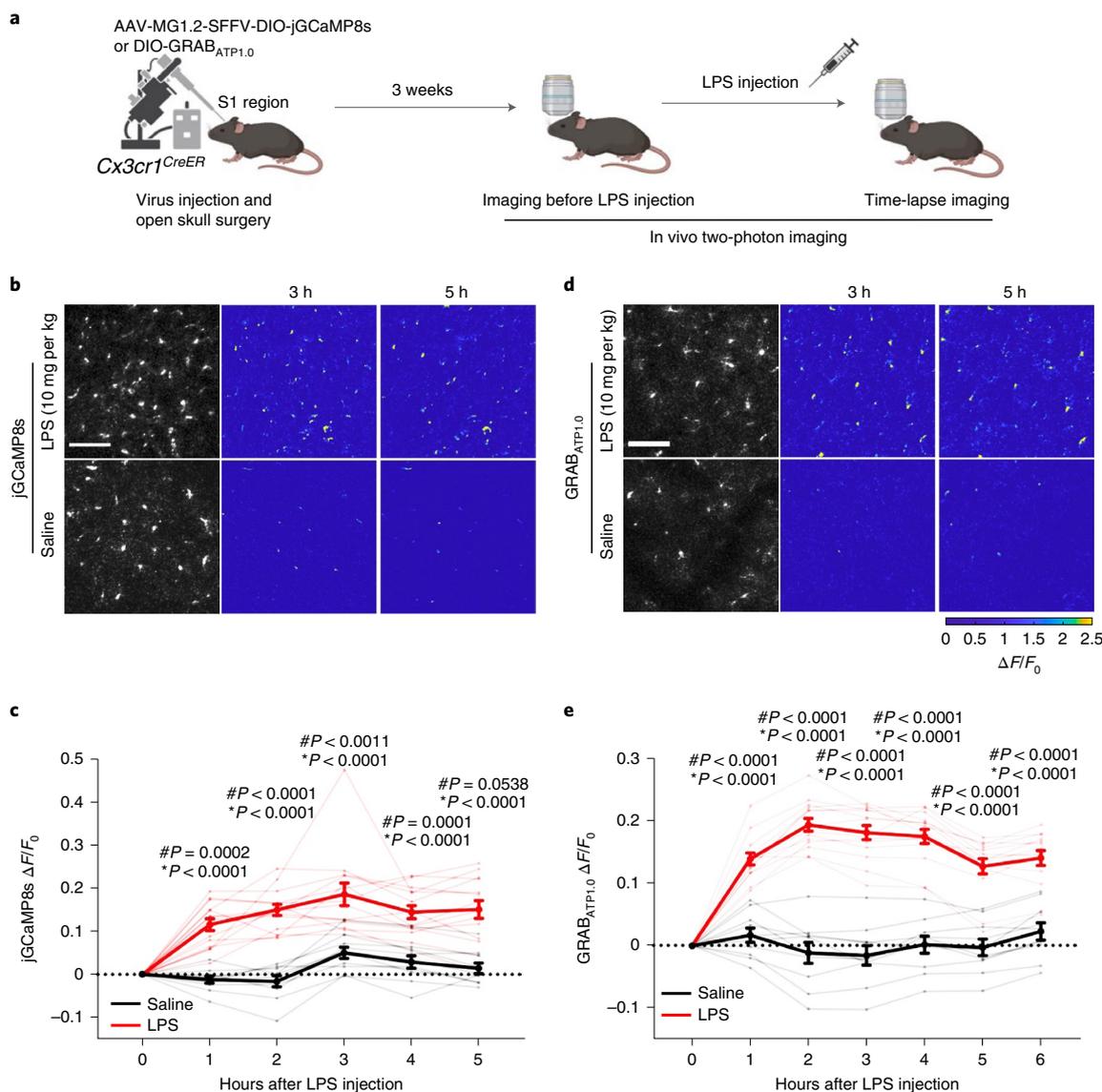
Fig. 4 | AAV-MGs enable in vivo two-photon imaging of microglial Ca²⁺ signal and ATP transmission. a, Schematic diagram showing the experimental procedure for in vivo two-photon imaging of calcium signal and ATP transmission. **b,d**, Representative images showing jGCaMP8s (**b**) and GRAB_ATP1.0 (**d**) expression in microglia, and heatmaps showing the jGCaMP8s (**b**) and GRAB_ATP1.0 (**d**) fluorescence signals at 3 and 5 h after LPS or saline injection. Scale bar, 100 μm. **c,e**, Quantification of jGCaMP8s (**c**) and GRAB_ATP1.0 (**e**) fluorescence signals at microglial somata after LPS ($n = 14$ cells) or saline ($n = 10$ cells) i.p. injection (two-way ANOVA: #Tukey's post-hoc versus 0 h; *Sidak's post-hoc versus saline; P values as listed in the figure). Data are given as mean ± s.e.m. F_0: mean fluorescence intensity in the baseline imaging session; ΔF: mean fluorescence intensity in the experimental imaging session − F_0.

Cre-dependent AAV vector that bears the calcium indicator jGCaMP8s[49]. We injected the rAAVs into the primary somatosensory (S1) cortex of *Cx3cr1^CreER* mice (Extended Data Fig. 9a). After waiting for 2 weeks to enable viral transgene expression, we used intraperitoneal (i.p.) injection of LPS (10 mg kg⁻¹) to induce systemic inflammation, and performed two-photon imaging to track the Ca²⁺ signals in the somata of microglia (Fig. 4a). We observed a significant increase in Ca²⁺ signals at 1 hour after LPS injection (Fig. 4b,c; P values are listed in the figure; two-way ANOVA with Tukey's post-hoc test). This LPS-induced elevation of intracellular Ca²⁺ was sustained and peaked at 3 hours after injection, and then started to decrease (Fig. 4b,c). The increase of Ca²⁺ signals was not caused by the i.p. injection procedure per se, given that the i.p. injection of saline did not lead to a jGCaMP8s fluorescence increase (Fig. 4b,c).

We also used AAV-MG1.2 to express the ATP fluorescent sensor GRAB_ATP1.0 (ref. [50]) in microglia in the S1 cortex of *Cx3cr1^CreER* mice

(Extended Data Fig. 9b) and performed in vivo two-photon imaging to monitor the GRAB fluorescence signals. We first examined the extracellular ATP changes at microglial somata following LPS i.p. injection (10 mg kg⁻¹) (Fig. 4a). Similar to the jGCaMP8s imaging experiment described above, LPS injection induced a significant increase of GRAB fluorescence signals at 1 hour after injection (Fig. 4d,e; P values are listed in the figure; two-way ANOVA with Tukey's post-hoc test). The fluorescence signals plateaued at 2 hours after injection and remained at a high level at 6 hours after injection (Fig. 4d,e). We did not observe a signal increase after i.p. saline injection (Fig. 4d,e), again indicating that the elevated GRAB fluorescence signals were not due to the i.p. injection procedure. We also examined the extracellular ATP changes at microglial somata upon acute tissue damage. We applied a brief laser ablation to induce local tissue damage, and found an immediate increase in GRAB fluorescence signals that continued to ramp up for up to 40 min (Extended Data Fig. 9c,d).
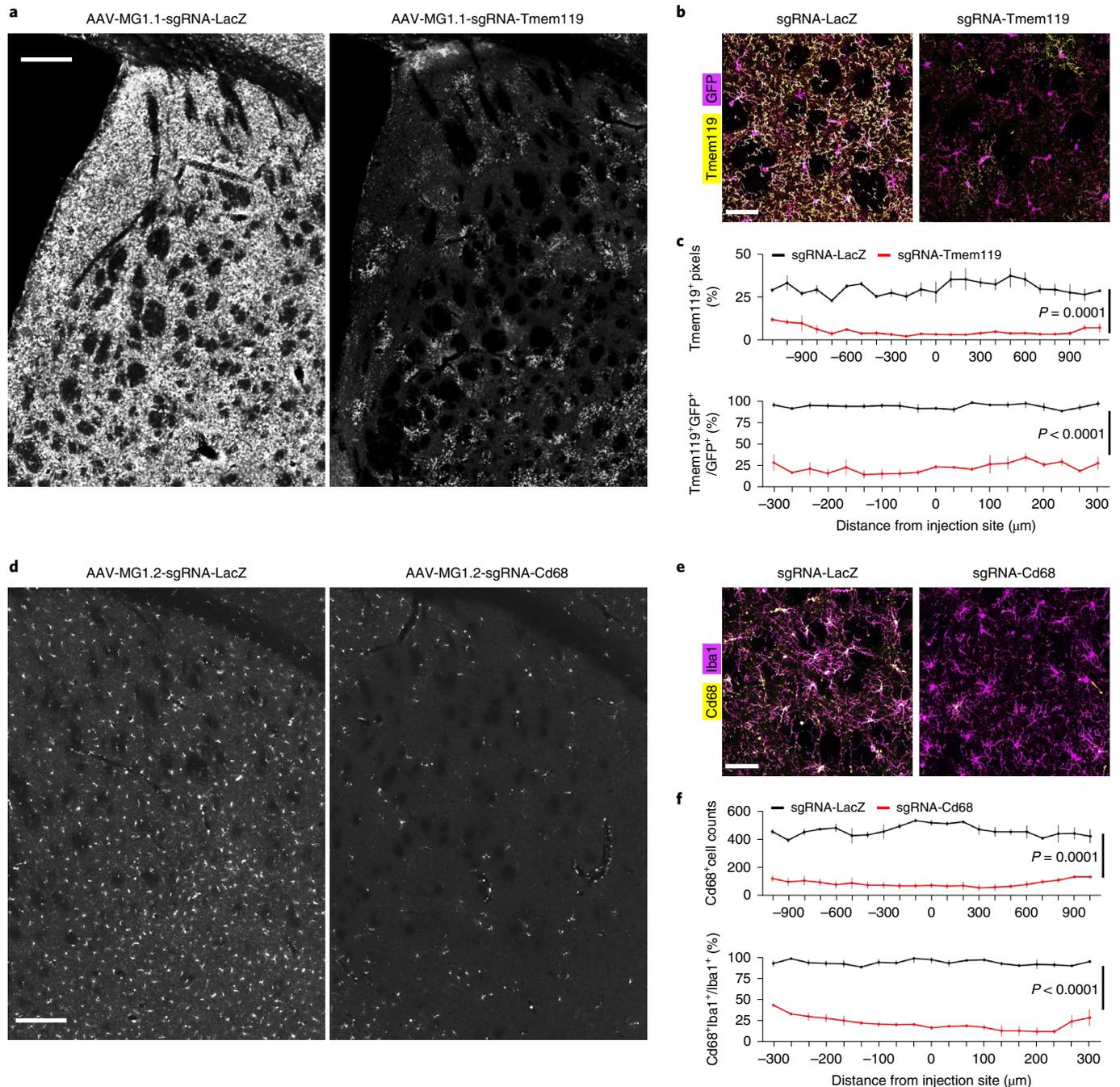
Fig. 5 | AAV-MGs mediate efficient genome editing of microglia in vivo. a, Representative immunofluorescence images of the striatum of *Cx3cr1*[CreER]:*Rosa26-LSL-Cas9-GFP* mice injected with AAV-MG1.1-sgRNA-LacZ or AAV-MG1.1-sgRNA-Tmem119. The brain sections were immunostained against Tmem119. Scale bar, 200 μm. **b**, Representative images showing the colocalization of Tmem119 and GFP immunosignals in the striatum of *Cx3cr1*[CreER]:*Rosa26-LSL-Cas9-GFP* mice injected with AAV-MG1.1-sgRNA-LacZ or AAV-MG1.1-sgRNA-Tmem119. Scale bar, 100 μm. **c**, Quantification of the percentage of Tmem119-positive pixels and the percentage of Tmem119-positive microglia in a 1.5×1.5 mm^2 region in the dorsal striatum (*n* = 3 mice for each group; two-way ANOVA; *P* values as listed in the figure). Data are given as mean ± s.e.m. **d**, Representative immunofluorescence images of the striatum of *Cx3cr1*[CreER]:*Rosa26-LSL-Cas9* mice injected with AAV-MG1.2-sgRNA-LacZ or AAV-MG1.2-sgRNA-Cd68. The brain sections were immunostained against Cd68. Scale bar, 200 μm. **e**, Representative images showing the colocalization of Cd68 and Iba1 immunosignals in the striatum of *Cx3cr1*[CreER]:*Rosa26-LSL-Cas9* mice injected with AAV-MG1.2-sgRNA-LacZ or AAV-MG1.2-sgRNA-Cd68. Scale bar, 100 μm. **f**, Quantification of the number of Cd68-positive cells and the percentage of Cd68-positive microglia in a 1×1 mm^2 region in the dorsal striatum (*n* = 3 mice for each group; two-way ANOVA; *P* values as listed in the figure). Data are given as mean ± s.e.m.

AAV-MGs mediate efficient microglia genome editing in vivo. We explored the utility of AAV-MGs for microglial genome editing. We crossed the Cre-dependent Rosa26 Cas9 reporter mouse (*Rosa26-LSL-Cas9-GFP*)[51] with the *Cx3cr1*[CreER] mouse. We induced the expression of *Streptococcus pyogenes* Cas9 in microglia by tamoxifen i.p. injection. We used AAV-MGs to package a single-stranded
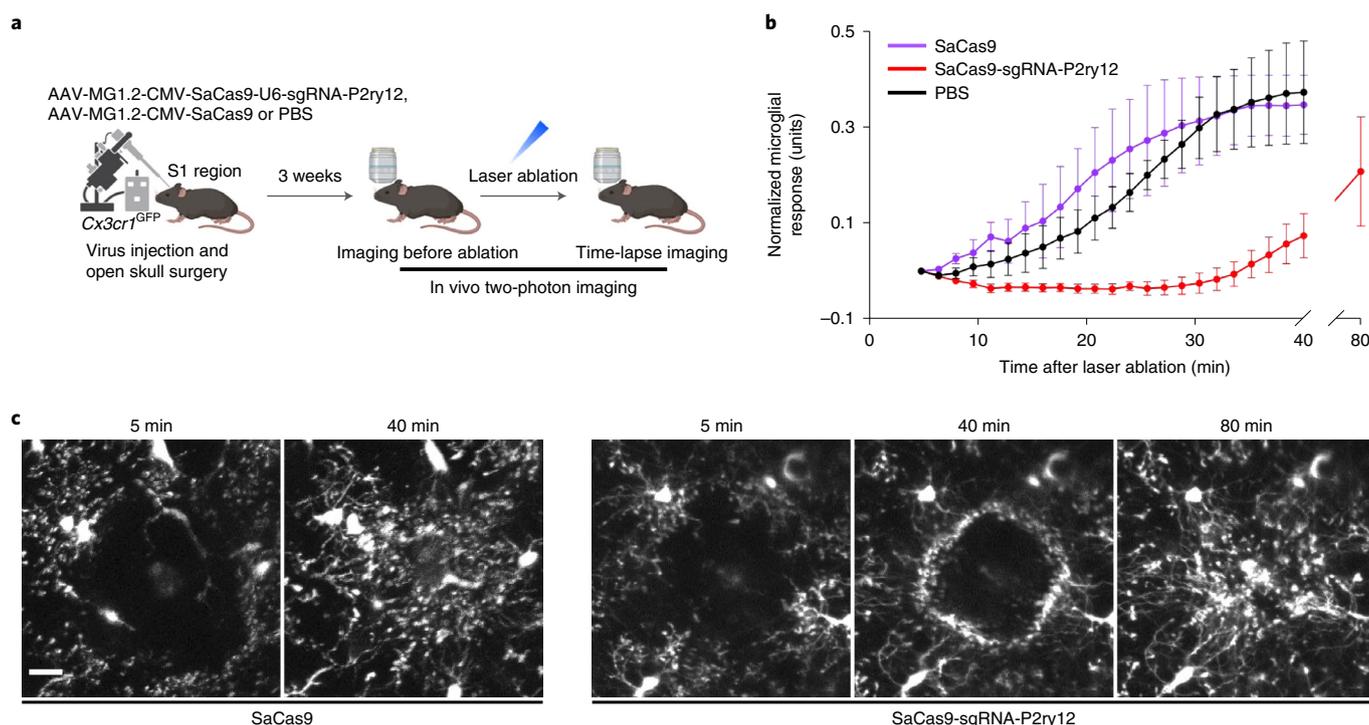
Fig. 6 | AAV-MG delivery of SaCas9 for in vivo genome editing in microglia. a, Schematic diagram showing the experimental procedure for in vivo two-photon imaging of microglial responses to laser ablation. **b**, Quantification of microglial process extension toward the laser ablation site in *Cx3cr1*^GFP mice injected with PBS (*n* = 3 fields from 3 mice), AAV-MG1.2-CMV-SaCas9 (*n* = 3 fields from 3 mice) or AAV-MG1.2-CMV-SaCas9-U6-sgRNA-P2ry12 (*n* = 6 fields from 3 mice). Data are given as mean ± s.e.m. **c**, Representative images showing the recruitment of microglial processes to the two-photon laser ablation site in *Cx3cr1*^GFP mice injected with AAV-MG1.2-CMV-SaCas9 or AAV-MG1.2-CMV-SaCas9-U6-sgRNA-P2ry12. Scale bar, 20 μm.

AAV vector that expresses a single guide RNA (sgRNA) and chose two microglia-specific genes, *Tmem119* and *Cd68*, as the targets for editing. An rAAV harboring an sgRNA targeting *LacZ* served as the control virus. Four weeks after injecting the rAAVs into the striatum, we examined the knockout efficiency by immunostaining. For both target genes, the immunofluorescence signals of their encoded proteins were reduced by >70% in the striatum of the mouse brains injected with the knockout rAAVs but not in the mouse brains injected with the control rAAVs (Fig. 5 and Extended Data Fig. 10a,b). We achieved effective knockout of target genes over a large area in the dorsal striatum along the anterior–posterior axis by a single AAV injection (Fig. 5a,c,d,f and Extended Data Fig. 10a,b).

To further demonstrate direct microglia genome editing in vivo, we used AAV-MG1.2 to express a miniaturized Cas9 (*Staphylococcus aureus* Cas9, SaCas9, ref. [52]) and an sgRNA from a single AAV vector in microglia. We designed an sgRNA targeting the microglia homeostatic marker gene *P2ry12*, which is essential for microglia to detect extracellular nucleotides[4]. A single injection of this rAAV in the S1 cortex of *Cx3cr1*^GFP transgenic mice, which selectively express green fluorescent protein (GFP) in microglia, led to knockout of *P2ry12* over a large area as evidenced by depleted immunostaining signals (Extended Data Fig. 10c,d). Expressing the SaCas9 without an sgRNA did not affect endogenous *P2ry12* expression (Extended Data Fig. 10c,d), demonstrating that the observed *P2ry12* knockout was not due to AAV-MG-induced microglial activation[4] and that the gene knockout by SaCas9 requires a specific sgRNA.

Finally, we examined the physiological consequences of AAV-MG1.2-mediated *P2ry12* knockout. Four weeks after PBS or virus injection into the S1 cortex of *Cx3cr1*^GFP transgenic mice, we performed in vivo two-photon imaging to track the morphological responses of microglia to tissue damage (Fig. 6a). Focal laser ablation in the mouse brains injected with the control rAAV or PBS induced immediate extension and recruitment of microglial processes towards the damage site, which reached peak magnitude in 30–40 min after ablation (Fig. 6b,c). In contrast, the chemotactic responses of microglia from those mouse brains injected with the *P2ry12*-knockout rAAV were reduced: microglial responses started only after ~30 min and reached peak magnitude after ~80 min following focal laser ablation (Fig. 6b,c). These results are consistent with a previous study using *P2ry12*-deficient transgenic mice[4]. The AAV-based gene knockout approach circumvents the potential confounding effects of *P2ry12* deficiency during development, and thus these results further support a role of *P2ry12* in guiding microglial chemotaxis.

Discussion

Our development of engineered AAV capsids that are capable of efficient microglial transduction provides much-needed viral tools for the investigation of microglia biology. We have demonstrated that AAV-MGs enable sufficient transgene expression in microglia for labeling, monitoring and manipulation. Also, combining AAV-MGs with other rAAVs targeting additional cell types in the CNS represents a promising strategy to study the interactions between microglia and different cell types in the same animal.

Recent single-cell transcriptomics studies have demonstrated a high level of regional heterogeneity of microglia in the brain[53,54]. AAV-MGs are suitable tools for brain region-specific microglia manipulation in vivo to investigate the roles of microglia in controlling neural circuits in different brain areas. Genetic studies in human patients identified druggable targets and signaling pathways of CNS diseases that are highly enriched in microglia[21,53,55]. Our AAV capsids can effectively and safely transduce microglia and lay the foundation for future studies using various in vivo genome editing technologies to investigate disease progression.

In this study, we used microglia-specific Cre lines to achieve microglia-specific viral transgene expression in vivo. Multiple Cre lines have been generated recently to target microglia and microglia subtypes[42,56,57]. Combining AAV-MGs with these transgenic lines opens up possibilities for in vivo microglia studies. Notably, careful control experiments should be performed to examine the possible effects of Cre induction on microglia development[58]. A promising future direction is to identify and use *Cis*-regulatory elements with sizes that are compatible with AAV packaging capacity to restrict AAV-MG-mediated transgene expression in microglia in wild-type animals. So far, no enhancer or promoter is widely accepted in the field as microglia specific for viral transgene expression. Our AAV-MGs provide a critical platform for future studies to identify and rigorously test such *Cis*-regulatory elements.

Online content

Any methods, additional references, Nature Research reporting summaries, source data, extended data, supplementary information, acknowledgements, peer review information; details of author contributions and competing interests; and statements of data and code availability are available at https://doi.org/10.1038/s41592-022-01547-7.

References

1. Colonna, M. & Butovsky, O. Microglia function in the central nervous system during health and neurodegeneration. *Annu. Rev. Immunol.* **35**, 441–468 (2017).
2. Prinz, M., Jung, S. & Priller, J. Microglia biology: one century of evolving concepts. *Cell* **179**, 292–311 (2019).
3. Nimmerjahn, A., Kirchhoff, F. & Helmchen, F. Resting microglial cells are highly dynamic surveillants of brain parenchyma in vivo. *Science* **308**, 1314–1318 (2005).
4. Haynes, S. E. et al. The P2Y12 receptor regulates microglial activation by extracellular nucleotides. *Nat. Neurosci.* **9**, 1512–1519 (2006).
5. Davalos, D. et al. ATP mediates rapid microglial response to local brain injury in vivo. *Nat. Neurosci.* **8**, 752–758 (2005).
6. Stevens, B. et al. The classical complement cascade mediates CNS synapse elimination. *Cell* **131**, 1164–1178 (2007).
7. Stephan, A. H., Barres, B. A. & Stevens, B. The complement system: an unexpected role in synaptic pruning during development and disease. *Annu. Rev. Neurosci.* **35**, 369–389 (2012).
8. Parkhurst, C. N. et al. Microglia promote learning-dependent synapse formation through brain-derived neurotrophic factor. *Cell* **155**, 1596–1609 (2013).
9. Nguyen, P. T. et al. Microglial remodeling of the extracellular matrix promotes synapse plasticity. *Cell* **182**, 388–403 (2020).
10. Badimon, A. et al. Negative feedback control of neuronal activity by microglia. *Nature* **586**, 417–423 (2020).
11. Merlini, M. et al. Microglial G$_i$-dependent dynamics regulate brain network hyperexcitability. *Nat. Neurosci.* **24**, 19–23 (2021).
12. Pluvinage, J. V. et al. CD22 blockade restores homeostatic microglial phagocytosis in ageing brains. *Nature* **568**, 187–192 (2019).
13. Hong, S. et al. Complement and microglia mediate early synapse loss in Alzheimer mouse models. *Science* **352**, 712–716 (2016).
14. Keren-Shaul, H. et al. A unique microglia type associated with restricting development of Alzheimer's disease. *Cell* **169**, 1276–1290 (2017).
15. Mathys, H. et al. Single-cell transcriptomic analysis of Alzheimer's disease. *Nature* **570**, 332–337 (2019).
16. Keane, L., Cheray, M., Blomgren, K. & Joseph, B. Multifaceted microglia: key players in primary brain tumour heterogeneity. *Nat. Rev. Neurol.* **17**, 243–259 (2021).
17. Gutmann, D. H. & Kettenmann, H. Microglia/brain macrophages as central drivers of brain tumor pathobiology. *Neuron* **104**, 442–449 (2019).
18. Shen, X. et al. Glioma-induced inhibition of caspase-3 in microglia promotes a tumor-supportive phenotype. *Nat. Immunol.* **17**, 1282–1290 (2016).
19. Guerreiro, R. et al. TREM2 variants in Alzheimer's disease. *N. Engl. J. Med.* **368**, 117–127 (2013).
20. Jonsson, T. et al. Variant of TREM2 associated with the risk of Alzheimer's disease. *N. Engl. J. Med.* **368**, 107–116 (2013).
21. Lewcock, J. W. et al. Emerging microglia biology defines novel therapeutic approaches for Alzheimer's disease. *Neuron* **108**, 801–821 (2020).
22. Bedbrook, C. N., Deverman, B. E. & Gradinaru, V. Viral strategies for targeting the central and peripheral nervous systems. *Annu. Rev. Neurosci.* **41**, 323–348 (2018).
23. Jüttner, J. et al. Targeting neuronal and glial cell types with synthetic promoter AAVs in mice, non-human primates and humans. *Nat. Neurosci.* **22**, 1345–1356 (2019).
24. Sahel, J.-A. et al. Partial recovery of visual function in a blind patient after optogenetic therapy. *Nat. Med.* **27**, 1223–1229 (2021).
25. Cucchiarini, M., Ren, X. L., Perides, G. & Terwilliger, E. F. Selective gene expression in brain microglia mediated via adeno-associated virus type 2 and type 5 vectors. *Gene Ther.* **10**, 657–667 (2003).
26. Rosario, A. M. et al. Microglia-specific targeting by novel capsid-modified AAV6 vectors. *Mol. Ther. Methods Clin. Dev.* **3**, 16026 (2016).
27. Su, W. et al. Recombinant adeno-associated viral (rAAV) vectors mediate efficient gene transduction in cultured neonatal and adult microglia. *J. Neurochem.* **136**, 49–62 (2016).
28. Maes, M. E., Colombo, G., Schulz, R. & Siegert, S. Targeting microglia with lentivirus and AAV: recent advances and remaining challenges. *Neurosci. Lett.* **707**, 134310 (2019).
29. O'Carroll, S. J., Cook, W. H. & Young, D. AAV targeting of glial cell types in the central and peripheral nervous system and relevance to human gene therapy. *Front. Mol. Neurosci.* **13**, 618020 (2021).
30. Maes, M. E., Wögenstein, G. M., Colombo, G., Casado-Polanco, R. & Siegert, S. Optimizing AAV2/6 microglial targeting identified enhanced efficiency in the photoreceptor degenerative environment. *Mol. Ther. Methods Clin. Dev.* **23**, 210–224 (2021).
31. Klichinsky, M. et al. Human chimeric antigen receptor macrophages for cancer immunotherapy. *Nat. Biotechnol.* **38**, 947–953 (2020).
32. Raupp, C. et al. The threefold protrusions of adeno-associated virus type 8 are involved in cell surface targeting as well as postattachment processing. *J. Virol.* **86**, 9396–9408 (2012).
33. Kronenberg, S., Kleinschmidt, J. A. & Böttcher, B. Electron cryo-microscopy and image reconstruction of adeno-associated virus type 2 empty capsids. *EMBO Rep.* **2**, 997–1002 (2001).
34. DiMattia, M. A. et al. Structural insight into the unique properties of adeno-associated virus serotype 9. *J. Virol.* **86**, 6947–6958 (2012).
35. Ransohoff, R. M. A polarizing question: do M1 and M2 microglia exist? *Nat. Neurosci.* **19**, 987–991 (2016).
36. Suzumura, A., Sawada, M., Itoh, Y. & Marunouchi, T. Interleukin-4 induces proliferation and activation of microglia but suppresses their induction of class II major histocompatibility complex antigen expression. *J. Neuroimmunol.* **53**, 209–218 (1994).
37. Paulk, N. K., Loza, L. M., Finegold, M. J. & Grompe, M. AAV-mediated gene targeting is significantly enhanced by transient inhibition of nonhomologous end joining or the proteasome in vivo. *Hum. Gene Ther.* **23**, 658–665 (2012).
38. Nicolson, S. C., Li, C., Hirsch, M. L., Setola, V. & Samulski, R. J. Identification and validation of small molecules that enhance recombinant adeno-associated virus transduction following high-throughput screens. *J. Virol.* **90**, 7019–7031 (2016).
39. Monahan, P. E. et al. Proteasome inhibitors enhance gene delivery by AAV virus vectors expressing large genomes in hemophilia mouse and dog models: a strategy for broad clinical application. *Mol. Ther.* **18**, 1907–1916 (2010).
40. Gong, H. et al. Transduction catalysis: doxorubicin amplifies rAAV-mediated gene expression in the cortex of higher-order vertebrates. *iScience* **24**, 102685 (2021).
41. Deverman, B. E. et al. Cre-dependent selection yields AAV variants for widespread gene transfer to the adult brain. *Nat. Biotechnol.* **34**, 204–209 (2016).
42. Kaiser, T. & Feng, G. Tmem119-EGFP and Tmem119-CreERT2 transgenic mice for labeling and manipulating microglia. *eNeuro* **6**, ENEURO.0448-18.2019 (2019).
43. Zhang, S. et al. Single-cell transcriptomics identifies divergent developmental lineage trajectories during human pituitary development. *Nat. Commun.* **11**, 5275 (2020).
44. McInnes, L., Healy, J. & Melville, J. UMAP: uniform manifold approximation and projection for dimension reduction. Preprint at https://doi.org/10.48550/arxiv.1802.03426 (2018).
45. Blondel, V. D., Guillaume, J.-L., Lambiotte, R. & Lefebvre, E. Fast unfolding of communities in large networks. *J. Stat. Mech.* **2008**, P10008 (2008).
46. Aibar, S. et al. SCENIC: single-cell regulatory network inference and clustering. *Nat. Methods* **14**, 1083–1086 (2017).
47. Ndoja, A. et al. Ubiquitin ligase COP1 suppresses neuroinflammation by degrading c/EBPβ in microglia. *Cell* **182**, 1156–1169 (2020).
48. Hao, Y. et al. Integrated analysis of multimodal single-cell data. *Cell* **184**, 3573–3587 (2021).
49. Zhang, Y. et al. Fast and sensitive GCaMP calcium indicators for imaging neural populations. Preprint at https://doi.org/10.1101/2021.11.08.467793 (2021).

50. Wu, Z. et al. A sensitive GRAB sensor for detecting extracellular ATP in vitro and in vivo. *Neuron* **110**, 770–782 (2022).
51. Platt, R. J. et al. CRISPR-Cas9 knockin mice for genome editing and cancer modeling. *Cell* **159**, 440–455 (2014).
52. Ran, F. A. et al. In vivo genome editing using *Staphylococcus aureus* Cas9. *Nature* **520**, 186–191 (2015).
53. Priller, J. & Prinz, M. Targeting microglia in brain disorders. *Science* **365**, 32–33 (2019).
54. Stratoulias, V., Venero, J. L., Tremblay, M.-È. & Joseph, B. Microglial subtypes: diversity within the microglial community. *EMBO J.* **38**, e101997 (2019).
55. Ulland, T. K. & Colonna, M. TREM2: a key player in microglial biology and Alzheimer disease. *Nat. Rev. Neurol.* **14**, 667–675 (2018).
56. Masuda, T. et al. Novel Hexb-based tools for studying microglia in the CNS. *Nat. Immunol.* **21**, 802–815 (2020).
57. McKinsey, G. L. et al. A new genetic strategy for targeting microglia in development and disease. *eLife* **9**, e54590 (2020).
58. Sahasrabuddhe, V. & Ghosh, H. S. Cx3Cr1-Cre induction leads to microglial activation and IFN-1 signaling caused by DNA damage in early postnatal brain. *Cell Rep.* **38**, 110252 (2022).

Methods

Mice. Animal care and use followed the approval of the Animal Care and Use Committee of the National Institute of Biological Sciences, Beijing in accordance with the Regulations for the Administration of Affairs Concerning Experimental Animals of China. *Cx3cr1*[CreER] mice (cat. no. 021160, *Cx3cr1*[tm2.1(cre/ERT2)Litt]/WganJ), *Cx3cr1*[GFP] mice (cat. no. 005582, *Cx3cr1*[tm1Litt]/J), *Tmem119*[CreER] mice (cat. no. 031820, *Tmem119*[em1(cre/ERT2)Gfng]/J) and *Rosa26-LSL-Cas9-GFP* mice (cat. no. 024857, *Gt(ROSA)26Sor*[tm1(CAG-cas9*,-EGFP)Fezh]/J) mice were obtained from Jackson Laboratory. Adult mice (10–16 weeks) of either sex were used for in vivo virus injection. The postnatal day 1 and adult C57BL/6N wild-type mice (8–10 weeks) were obtained from Beijing Vital River Laboratory Animal Technology. Mice were maintained with a 12–12 h photoperiod (light on at 08:00) and were given food and water ad libitum. Ambient temperature was kept at 25 °C with humidity at 50%.

Plasmids. The amino acid sequences of the engineered capsids generated in this work were listed in Supplementary Table 4. The plasmids for capsid screening were constructed according to the CREATE protocol[41] with modifications. The pAAV-CMV-mScarlet-ΔCap-DIO-SV40pA plasmid contains an mScarlet[59] expression cassette, a *cis* Cap cassette and a DIO cassette. The mScarlet expression cassette consists of a cytomegalovirus (CMV) promoter, the mScarlet coding sequence and an SV40pA sequence. The *cis* Cap cassette includes the AAV5 p41 promoter sequence, the AAV2 *rep* splicing sequence and the AAV9 *cap* sequence. The AAV9 *cap* sequence was modified as previously reported[41] to introduce an XbaI site and an AgeI site for subsequent library generation. The DIO cassette contains an SV40pA sequence. The pCRII-9Cap-xE plasmid and the AAV2/9 REP-AAP helper plasmid were constructed following the original report[41].

The pAAV-SFFV backbone was constructed by replacing the Ef1a promoter of the pAAV-DIO-hChR2(H134R)-mCherry (Addgene, cat. no. 20297) with the SFFV promoter from the pHR-SFFV plasmid (Addgene, cat. no. 46911). The mScarlet coding sequence was subcloned into the DIO cassette to make the pAAV-SFFV-DIO-mScarlet plasmid, or was subcloned after the SFFV promoter to make the pAAV-SFFV-mScarlet plasmid. To make the pAAV-SFFV-DIO-jGCaMP8s plasmid, the jGCaMP8s (Addgene, cat. no. 162380; HA-tag at C-terminal) coding sequence was synthesized and subcloned into the DIO cassette. The GRAB[ATP1.0] was developed as described[50] and subcloned into the pAAV-SFFV-DIO backbone. The pAAV-U6-sgRNA-SFFV-DIO-mScarlet plasmid was constructed by replacing the hSyn-Cre-2A-GFP-KASH cassette on the original plasmid (Addgene, cat. no. 60231) with the DIO-mScarlet cassette. The sgRNAs targeting *Tmem119* (5′-GGGACCCCGTACCTTCAGCG) and *Cd68* (5′-ATCCTATACCCAATTCAGGG) were selected from the mouse Brie CRISPR knockout sgRNA library (Addgene, cat. no. 73632), which includes four sgRNAs for each gene. We chose the ones that have the highest 'rule set 2' score. The sgRNAs were synthesized and cloned into the pAAV-U6-sgRNA-SFFV-DIO-mScarlet plasmid. The SaCas9 sgRNAs targeting exon 4 of *P2ry12* (5′-CGGCTCCCAGTTTAGCATCACT) were designed using the web tool Benchling (https://benchling.com/crispr), and subsequently synthesized and cloned into the original pX601 plasmid[52] following the SaCas9 user manual.

To minimize the potential spontaneous recombination during bacterial growth, Stbl3 cell lines were used to amplify AAV vectors that contain DIO cassettes.

AAV packaging. The AAV vectors were packaged as previously described[41,60,61]. The detailed protocol is reported in ref.[62]. In brief, the AAV vectors and the AAV helper plasmids were co-transfected into HEK293T cells. Cells were collected 96 h after transfection, and the viral particles were released from cells by freeze–thaw cycling and sonication. The virus was purified using cesium chloride density-gradient ultracentrifugation and dialyzed into PBS buffer. The viral titer was analyzed using quantitative polymerase chain reaction (qPCR). The sequences of primers for virus titering are listed in Supplementary Table 5. The typical yields of AAV production using AAV-cMG, AAV-MG1.1 or AAV-MG1.2 are listed in Supplementary Table 6.

Mouse microglia isolation and culture. Primary mouse microglia cells were obtained from postnatal day 1 C57BL/6 wild-type mice. Pups were placed on ice for 1–2 min until they were unresponsive, then were soaked with 75% alcohol and were carefully decapitated. Brains were collected with clean sterile scissors and placed in a 10 cm dish containing 10 ml iced dissociation medium (DMEM/F12 (Gibco cat. no. 11330032) supplemented with 100 U ml⁻¹ penicillin and 100 μg ml⁻¹ streptomycin (P/S, Gibco cat. no. 15140-122)). All meninges were removed using No. 5 Dumont forceps under a dissecting microscope. Brains were mechanically dissociated in dissociation medium. Dissociated cells were filtered through a 40 μm cell strainer and centrifuged at 200 ×*g* for 10 min at 25 °C. Pellets were resuspended with culture medium (DMEM/F12 supplemented with 10% fetal bovine serum (FBS, Gibco cat. no. 0099-141), 5 ng ml⁻¹ granulocyte–macrophage colony-stimulating factor (GM-CSF, Abbkine cat. no. PRP100489) and 1% P/S) and plated at a density of five brains per T-75 plastic culture flask (Falcon) pre-coated with poly-L-lysine (Sigma-Aldrich, cat. no. P8920). The culture medium was changed 24 h after isolation. After that, 50% of the culture medium was changed every 3 days. Two weeks later the flasks were shaken at 180 r.p.m. using an orbital

shaker for 2 h at 37 °C to collect microglia. Cultured microglia were maintained at 37 °C in a humidified incubator with 5% CO₂.

In vitro screening. The screening of AAV variants in cultured mouse microglia was based on the CREATE protocol[41] with modifications (without using the Cre-dependent mechanism). The sequence of primers used in the screening is listed in Supplementary Table 2. We first constructed an AAV capsid library by inserting random heptamers between the 588 and 589 sites of the AAV9 VP1 protein (Fig. 1a). The inserted peptides are also present in both the VP2 and VP3 proteins because this insertion site is located in a region common to VP1, VP2 and VP3[34]. In brief, the library fragments were generated by PCR using the XF and 7xMNN primers with the pCRII-9Cap-xE plasmid serving as the template. The pAAV-CMV-mScarlet-ΔCap-DIO-SV40pA plasmid was linearized by XbaI and AgeI. The library fragments were assembled into the linearized pAAV-CMV-mScarlet-ΔCap-DIO-SV40pA plasmid using Gibson assembly. The resulting library (theoretical library size: 3.4 × 10¹⁰ unique nucleotide sequences) was packaged into rAAVs by co-transfecting the AAV capsid library, the AAV2/9 REP-AAP helper plasmid and the AAV helper plasmid into HEK293T cells. Approximately 1.2 × 10¹⁰ library rAAVs (2 × 10⁶ viral genomes (vg) μl⁻¹, 6 ml) were used to transduce the cultured mouse microglia for 24 h. At 48 h after transduction, the genomes of rAAVs that had successfully transduced the cultured microglia were recovered using Trizol. The *cap* sequences were first amplified from recovered AAV genomes by PCR using used the 9CapF and SV40pA-R primers. The PCR product was purified and used as the template for the second PCR reaction that used the XF and 588i-R primers. The recovered *cap* sequences were then assembled back into the pAAV-CMV-mScarlet-ΔCap-DIO-SV40pA plasmid. The variants recovered from the first round of screening were packaged into rAAVs (1.5 × 10⁶ vg μl⁻¹, 1 ml) and screened again in the cultured mouse microglia.

The recovered variants from both rounds were sequenced to a depth of ~8 million reads. A total of 696 unique inserted heptamer sequences that were detected in more than one read in both rounds were identified. To assess the enrichment of these inserted peptides after two rounds of selection, two parameters were calculated for each heptamer sequence. The first parameter is the fold change of the normalized read count between round 2 and round 1 (that is, enrichment score). The enrichment score of a variant is calculated as follows:

$$\text{Enrichment score} = \log_{10}$$

$$((\text{normalized read counts in round 2}) / (\text{normalized read counts in round 1})).$$

The second parameter is the read frequency in the total of the round 2 reads (that is, round 2 read percentage). The round 2 read percentage of a variant is calculated as follows:

$$\text{Round 2 read percentage} =$$
read counts in round 2/total read counts of all variants in round 2.

All recovered heptamer insertions were ranked using these two parameters (Supplementary Table 1). Two rankings were not entirely matched, and no apparent consensus motifs were found among the top 10 variants in both rankings. Therefore, variants that ranked in the top 10 for both parameters were chosen, and packaged individually into rAAVs for further tests. In the initial experiment, AAV-cMG.WPP and AAV-cMG.QRP were identified as showing highly efficient transduction to cultured mouse microglia.

To obtain variants that mediate even higher in vitro microglial transduction, we constructed an AAV-cMG.QRP capsid mutant library in which the inserted heptamer and the four flanking amino acids in the AAV-cMG.QRP capsid were randomized (Fig. 1c). In brief, the library fragments were generated by 10 separate PCR reactions using the XF and QRP-mut-R1-10 primers with the pCRII-9Cap-xE plasmid serving as the template. Equal amounts of 10 PCR products were mixed and assembled into the pAAV-CMV-mScarlet-ΔCap-DIO-SV40pA plasmid using the Gibson assembly. The resulting library (theoretical library size: 3.8 × 10⁷ unique nucleotide sequences) was packaged into rAAVs (1 × 10⁷ vg μl⁻¹, 1 ml) and screened in cultured muse microglia for one round as described above. A total of 10% of the rAAVs from the library of AAV-cMG.QRP variants were sequenced to a depth of ~12 million reads, and the recovered variants were sequenced to a depth of ~5.5 million reads. A total of 1,039 unique 11-mer sequences (including the original AAV-cMG.QRP) were detected for more than one read in both the library and the recovered sample. We ranked the recovered variants (Supplementary Table 1) and chose candidates for further tests as described above. Screening a similar AAV-cMG.WPP variants library in cultured mouse microglia did not generate variants with improved in vitro performance compared with AAV-cMG.

In vitro AAV transduction. Microglia were plated in 96-well cell culture plates (PerkinElmer, cat. no. 6005550). Microglia were transduced with rAAVs packaged using candidate capsids at a multiplicity of infection (MOI) of 10,000. After 2 days the culture medium was changed to the TIC medium[62] (DMEM/F12 supplemented with 1% P/S, 2 mM L-glutamine (Gibco, cat. no. 25030-081), 5 mg ml⁻¹ *N*-acetyl cysteine (Sigma-Aldrich, cat. no. A9165), 5 mg ml⁻¹ insulin (Sigma-Aldrich, cat. no. I0516), 100 mg ml⁻¹ apo-transferrin (Sigma-Aldrich, cat. no. T1147), 100 ng ml⁻¹ sodium selenite (Sigma-Aldrich, cat. no. S5261), 2 ng ml⁻¹

recombinant murine TGF-β2 (Sino Biological, cat. no. 50153-M08H), 100 ng ml⁻¹ recombinant murine IL-34 (Sino Biological, cat. no. 50055-M08H) and 1.5 mg ml⁻¹ cholesterol (ovine wool, Merck cat. no. 700000P)). Fluorescence imaging was performed and analyzed using the Opera Phenix High Content Screening System (PerkinElmer) 3 and 5 days after the transduction of rAAVs. To examine the effects of DOX on AAV-cMG transduction at the MOI of 1,000 or 10,000 (Fig. 1h,i), DOX (0.1 µg ml⁻¹; Sigma-Aldrich cat. no. D1515) was added to the medium before rAAV transduction.

Cultured microglia RNA sequencing. Mouse primary microglia were exposed to 200 ng ml⁻¹ LPS (Sigma-Aldrich cat. no. L4130) or 20 ng ml⁻¹ recombinant murine IL-4 (PeproTech, cat. no. 214-14) in TIC medium for 24 h. Total RNAs of treated microglia were extracted using Trizol (Thermo Fisher Scientific, cat. no. 15596018) and analyzed using single-end 75 bp high-throughput sequencing on an Illumina platform.

In vivo screening. The screening of in vivo AAV variants was performed using the CREATE protocol[41]. To identify AAV-MG.WPP variants that effectively transduced mouse microglia in vivo, we constructed an AAV-MG.WPP capsid mutant library in which the inserted heptamer and the four flanking amino acids in the AAV-MG.WPP capsid were randomized (Fig. 2a). In brief, the library fragments were generated by 10 separate PCR reactions using the XF and WPP-mut-R1-10 primers with the pCRII-9Cap-xE plasmid serving as the template. Equal amounts of 10 PCR products were mixed and assembled into the pAAV-CMV-mScarlet-ΔCap-DIO-SV40pA plasmid using the Gibson assembly. The resulting library (theoretical library size: 3.8×10^7 unique nucleotide sequences) was packaged into rAAVs as described above. We injected the library rAAVs (5×10^7 vg µl⁻¹) bilaterally into the striatum (800 nl) and the midbrain (500 nl) of three $Cx3cr1^{CreER}$ mice. Tamoxifen was injected (i.p., 100 mg kg⁻¹) for 5 consecutive days after virus injection. The mice were sacrificed 10 days after virus injection. The brains were dissected and the genomes of rAAVs that had successfully transduced cells in vivo were recovered using Trizol. The *cap* sequences in the Cre-recombined genomes were selectively amplified using the 9CapF and CDF primers. The candidates that were highly enriched were identified using next-generation sequencing and individually tested as described above (Supplementary Table 1). Screening a similar AAV-cMG.QRP variants library in cultured mouse microglia did not generate variants with improved in vivo performance compared with AAV-MGs.

Preparation of next-generation sequencing samples. Library rAAVs were treated with proteinase K at 37 °C overnight. The AAV genomes were obtained by phenol chloroform extraction and ethanol precipitation. A total of 100 ng AAV genomes were used as the PCR template. The *cap* fragments that contain the inserted heptamers were amplified using the 588i-F and 588i-R primers. The PCR products were purified and used as the template for the second PCR using the 1527 and 1532 primers. A final PCR was performed to add unique indices for subsequent next-generation sequencing using standard indexed primers. The indexed PCR products were size selected by 2% agarose gel before undergoing next-generation sequencing.

For in vivo selection, the *cap* sequences in the Cre-recombined AAV genomes were selectively amplified using the 9CapF and CDF primers. The *cap* fragments that contain the inserted heptamers were then amplified and indexed as described above.

Common surgery and virus injection. Mice were anesthetized with pentobarbital (i.p., 80 mg kg⁻¹) before surgery and then placed in a mouse stereotaxic instrument. Detailed information on the virus injections is given in Supplementary Table 3.

Injections were performed using a microsyringe pump (Nanoliter 2010 Injector, WPI) and a Micro4 controller (WPI). The virus was delivered to the target areas at a rate of 46 nl min⁻¹. DOX (150 ng g⁻¹) was injected retro-orbitally immediately after virus injection. All subsequent experiments were performed at least 2 weeks after virus injection, except for those involving in vivo CRISPR/Cas9 knockout, which were performed at least 3 weeks after virus injection. For $Cx3cr1^{CreER}$ mice, i.p. injection of tamoxifen was done for 3 consecutive days (5 consecutive days for the in vivo screening described above) after virus injection.

Isolation of single cells for microglia single-cell RNA sequencing. Mice received saline, LPS (0.83 mg kg⁻¹) or Poly(i:c) (10 mg kg⁻¹) injection 6 h before microglia collection. To minimize ex vivo activation[63] we used a cold-mechanical dissociation protocol as described previously[64–66] with minor modifications. All procedures were performed on ice with cold buffers or in refrigerated centrifuge. Mice were deeply anesthetized and perfused. Brains were quickly removed and immersed in Dounce buffer (HBSS with HEPES + DNase + RNase inhibitor) and cut into smaller chunks. The tissue solution was quickly transferred to a 15 ml Dounce homogenizer and gently homogenized with a loose-fitting pestle ~10 times. The remaining tissue pieces were allowed to sediment and the supernatant containing the cell suspensions was collected in a new tube. New Dounce buffer was added to the sediment tissue and the homogenization was repeated for another round. The collected cell solution was centrifuged, resuspended and passed sequentially

through 70 µm and 30 µm pre-wet cell strainers to remove debris. The cells were centrifuged once more and resuspended in 37% stock isotonic Percoll (SIP). A Percoll gradient of HBSS/30%/37%(cells)/70% was used to enrich microglia by centrifugation at $200 \times g$ for 20 min with minimal acceleration and no brake. Cells in the interphase between 30% and 37% were carefully collected, washed and resuspended in 0.04% BSA in Dulbecco's PBS. Cells were then manually picked for Smart-seq or run through the 10× Genomics Chromium Single Cell 3′ v3 protocol, and were subsequently sequenced on the Illumina platform.

Smart-seq2-based scRNA-seq library construction and sequencing. Single microglia cells in BSA buffer (0.04% BSA (Amresco, cat. no. 0332) in HBSS buffer) were picked under a stereo fluorescence microscope using a mouth pipette. A modified single-cell tagged reverse transcription sequencing protocol was used to construct the scRNA-seq library as previously described[43]. In brief, cells were lysed and messenger RNAs were released into the lysis buffer containing barcoded reverse transcription primers. mRNAs were reverse transcribed into complementary DNA. After cDNA pre-amplification, single-cell transcriptomes tagged with different barcodes were pooled together. An additional four cycles of PCR were performed using biotin-modified primers to enrich the 3′ end of cDNAs. The amplicons were randomly sheared into ~300 bp fragments by sonication (Covaris) and purified using Dynabeads MyOne Streptavidin C1 (Invitrogen, cat. no. 65002). The purified fragments were then processed on the Illumina platform for sequencing of 150 bp pair-end reads.

Sequencing data processing and quality control. Reference datasets generated by the 10× Genomics platform were aligned to a pre-built GRCm38 reference genome using the 'cellranger count' command and combined using the 'cellranger aggr' command (Cell Ranger v3.1.0). The resulting feature–barcode matrix files were loaded into Seurat[48] (v4.0.2) and filtered with the following quality control criteria: remove cells with mitochondrial RNA greater than 10% and cells expressing more than 300 features, and remove features expressed in less than 10 cells. After quality control we ran the Seurat workflow with default parameters and retained bona fide microglia from the dataset by manually defining subsets of clusters showing consistently high expression of *Hexb*[56], using the CellSelector function over the UMAP embedding.

For the Smart-seq2 dataset, we adopted a protocol listed in the umi-tools documentation (https://umi-tools.readthedocs.io/en/latest/Single_cell_tutorial.html) in which the fastq files were demultiplexed with UMI-tools[67] (v1.1.2), aligned with STAR[68] (v2.5.4b) and quantified with featureCounts[69] (Subread v1.6.3). A minor modification was made to the 'umi_tools whitelist' procedure, in which we searched for 100 cells to obtain an extended whitelist, but 'washed' the whitelist by retaining only those cell barcodes actually used in library preparation steps, which we called 'ground truth barcodes'. In the 'umi_tools extract' step, only those reads containing the ground truth barcodes were kept, whereas reads with adapter contaminations or major sequencing errors were removed. For quality control, we computed library size, feature number, mitochondrial RNA percentage and ribosomal RNA percentage from the feature–cell matrix. The scater[70] (v1.18.6) quickPerCellQC function was used to identify and remove cell outliers based on these four metrics. The transduction of rAAVs in sequenced microglia was determined by the detection of the *mScarlet* reporter transcript.

Unsupervised analysis for dimension reduction and identification of microglia states. We used the Seurat workflow with default parameters on both the 10× reference dataset and the Smart-seq2 dataset. Standard principal component analysis for both datasets was computed and the dimension of the datasets was chosen as 40 (dims = 1:40). To identify microglia states, we first annotated the reference dataset by labeling microglia from control mice as 'homeostatic' and microglia from LPS-treated mice as 'reactive'. We then proceeded to find transfer anchors between the query (Smart-seq2) and the reference (10×) datasets in the principal component analysis space with the FindTransferAnchors function, and projected the query data onto the reference dataset with the MapQuery function. Furthermore, we merged the reference and query datasets, and re-ran UMAP dimension reduction on the merged dataset to obtain a de novo visualization in the UMAP space.

SCENIC analysis. Regulon analysis is performed using a python implementation of the SCENIC (single-cell regulatory network inference and clustering) pipeline, pySCENIC (v0.11.2), following the procedures described in published and online protocols[71]. Results from the SCENIC[46] analysis are further explored in Cytoscape (v3.2.0) using the iRegulon[72] plug-in (v1.3).

In vivo two-photon imaging. The rAAVs (1 µl) packaged using the AAV-MG1.1 or AAV-MG1.2 capsids were injected into layers II–IV of the primary somatosensory cortex (S1) of $Cx3cr1^{CreER}$ or $Cx3cr1^{GFP}$ mice at the age of 8 weeks. After 2 weeks a circular piece of the skull 3 mm in diameter centered over the virus injection site was carefully removed. A custom-designed steel head bar that included an imaging chamber was positioned over the craniotomy and affixed to the exposed skull with cyanoacrylate glue and dental cement. Mice were allowed to recover from the surgery for 1 week. Two-photon imaging was performed 100–150 µm below

the dura mater using a FluoView FVMPE-RS microscope (Olympus, ×25, 1.05 numerical aperture (NA) water-immersion lens). The laser was tuned to 920 nm and was maintained below 50 mW for jGCaMP8s and GRAB$_{ATP}$ imaging or below 40 mW for GFP imaging. Microglia were imaged using z-stacks, each of which consisted of 16 images spaced 2 μm apart (30 μm in total depth). Lateral shifts were corrected using ImageJ with the StackReg plug-in. Data quantification was conducted using customized Matlab scripts and the GraphPad Prism software.

To monitor jGCaMP8s and GRAB$_{ATP1.0}$ fluorescence signal changes following LPS challenge, a 636 × 636 μm^2 field of view (512 × 512 pixel resolution, 1.24 μm pixel^{-1}) was imaged at 1.5 frames per second (f.p.s.). A 10 min time-lapse imaging session (50 z-stacks) was first performed to record the baseline fluorescence. An i.p. injection of LPS (10 mg kg^{-1}) was then done. Immediately following LPS injection, additional 10 min imaging sessions (six sessions for jGCaMP8s imaging and seven sessions for GRAB$_{ATP1.0}$ imaging) were performed at 50 min intervals. A maximum projection was created for each stack. Microglial somata were manually selected. For a 10 min imaging session, the fluorescence intensity of a microglia soma was averaged across 25 z-stacks.

To monitor GRAB$_{ATP1.0}$ fluorescence signal changes following laser ablation, a 636 × 636 μm^2 field of view (512 × 512 pixel resolution) was imaged at 1.5 f.p.s. A circular area of 15 μm in diameter in the center of the imaging field was selected, and 70 pulses of a 920 nm laser (30 ms per pulse) at ~500 mW were applied to induce acute tissue damage. Immediately following laser ablation, 40 min time-lapse imaging (200 z-stacks) was performed. A maximum projection was created for each stack. Microglial somata were manually selected to calculate the fluorescence intensity.

To record the responses of GFP-expressing microglia to acute tissue damage, a 318 × 318 μm^2 field of view (512 × 512 pixel resolution, 0.62 μm pixel^{-1}) was imaged at 1.5 f.p.s. The acute tissue damage was induced as described above. Immediately following laser ablation, 40 min (control mice; 200 z-stacks) or 80 min (*P2ry12* knockout mice; 400 z-stacks) time-lapse imaging was performed. The normalized microglial response was computed as described[4].

Immunohistochemistry. Mice were anesthetized with an overdose of pentobarbital and perfused intracardially with PBS, followed by paraformaldehyde (PFA, 4% wt/vol in PBS). Brains were dissected and postfixed in 4% PFA for at least 4 h at 25 °C. Samples were then dehydrated in 30% sucrose solution. Brain sections (30 μm) were prepared on a Cryostat microtome (Leica, cat. no. CM1950). Sections were permeabilized with 0.3% Triton X-100 in PBS (PBST) and blocked in 2% BSA in PBST at 25 °C for 1 h. Sections were then incubated with primary antibodies (anti-Iba1, 1:500, cat. no. 019-19741, Wako; anti-TMEM119, 1:1000, cat. no. ab209064, Abcam; anti-CD68, 1:500, cat. no. ab53444, Abcam; anti-P2RY12, 1:100, cat. no. 848002, BioLegend; anti-HA, 1:500, cat. no. 11867423001, Roche) overnight at 4 °C. The anti-TMEM119, anti-CD68 and anti-P2RY12 antibodies are monoclonal and have been extensively validated in previous studies. Samples were washed three times in PBST and were then incubated with fluorescent secondary antibodies (Goat anti-rabbit-AF647, 1:1000, cat. no. 111-605-144, Jackson ImmunoResearch; Goat anti-rabbit-AF488, 1:1000, cat. no. 111-545-003, Jackson ImmunoResearch; Goat anti-rat-Cy5, 1:1000, cat. no. 112-175-143, Jackson ImmunoResearch) at 25 °C for 2 h.

For cultured microglia, cells were first washed in cold PBS and then fixed in 4% PFA for 10 min at 25 °C. After washing again in PBS, cells were permeabilized in PBST and blocked in 2% BSA in PBST at 25 °C for 20 min. Cells were then incubated with antibodies (anti-Iba1, 1:500, cat. no. 019-19741, Wako) at 25 °C for 2 h. Cells were washed three times in PBST and were then incubated with fluorescent secondary antibodies (Goat anti-rabbit-AF488, 1:1000, cat. no. 111-545-003, Jackson ImmunoResearch) at 25 °C for 1 h.

Image acquisition and analysis of fixed tissues. Confocal microscopy was performed on a Zeiss LSM880 confocal scanning microscope (Zen v2.3). For slide scanner imaging, we performed wide-field fluorescence imaging using the Olympus VS120 virtual microscopy slide scanning system (Olyvia) with a ×10 objective. Cell counting was performed using Imaris. To assess the effect of DOX on mScarlet expression, we used Imaris to measure the mean fluorescence intensity of labeled cells in the striatum on nine brain sections centered on the virus injection site. All brain samples were processed using the same protocol and imaged under the same conditions. To quantify the knockout efficiency of the *Tmem119* sgRNA, we calculated the percentage of Tmem119 immunosignal-positive pixels over an area of 1.5 × 1.5 mm^2 that covers the dorsal striatum using the 'Threshold' function in ImageJ. Given that Tmem119 immunofluorescence is evenly distributed in the striatum, we used the percentage of Tmem119-positive pixels as a proxy for Tmem119-positive cell count to assess the knockout efficiency. We also calculated the percentage of Tmem119 immunosignal-positive GFP-expressing cells (that is, Cas9-expressing microglia) over the same area using Imaris. To quantify the knockout efficiency of the *P2ry12* sgRNA, we calculated the percentage of signal-positive pixels over an area of 1 × 1 mm^2 that covers the S1 cortex using the 'Threshold' function in ImageJ. For *Cd68* knockout experiments, we quantified the number of Cd68 immunosignal-positive cells and the percentage of Cd68/Iba1 double-positive cells in an area of 1.5 × 1.5 mm^2 that covers the dorsal striatum using Imaris.

Statistics and reproducibility. Statistical significance was evaluated using Prism 9 (Graphpad). All fluorescence intensity, transduction rate, cell counting and immunostaining experiments were independently performed ≥3 times with similar results, except for the Iba1 co-staining experiment involving *Tmem119*^{CreER} mice shown in Extended Data Fig. 5c,d (1 experiment). The samples for the scRNA-seq experiment were collected once. The cultured microglia RNA-seq experiments were performed independently twice.

Reporting summary. Further information on research design is available in the Nature Research Reporting Summary linked to this article.

Data availability

All numerical source data are provided with this paper. The next-generation sequencing datasets reported in this work are available under the GEO accession number GSE197743. The GRCm38 reference genome assembly was downloaded from https://nov2020.archive.ensembl.org/Mus_musculus/Info/Index. The following plasmids are deposited to Addgene: rAAV2/cMG (184539), rAAV2/MG1.1 (184540), rAAV2/MG1.2 (184541), rAAV2/cMG.WPP (184542) and rAAV2/cMG.QRP (184543). The raw images generated in this study are not suitable for distribution through public repositories due to the large file size and are available from the corresponding authors upon request. Source data are provided with this paper.

Code availability

The codes and scripts for analysis of the sequencing data included in this paper are available at https://github.com/RuiyuRayWang/Lin_AAV_Microglia_public.

References

59. Bindels, D. S. et al. mScarlet: a bright monomeric red fluorescent protein for cellular imaging. *Nat. Methods* **14**, 53–56 (2017).
60. Shin, J.-H., Yue, Y. & Duan, D. Recombinant adeno-associated viral vector production and purification. *Methods Mol. Biol.* **798**, 267–284 (2012).
61. Lin, R. et al. Cell-type-specific and projection-specific brain-wide reconstruction of single neurons. *Nat. Methods* **15**, 1033–1036 (2018).
62. Bohlen, C. J. et al. Diverse requirements for microglial survival, specification, and function revealed by defined-medium cultures. *Neuron* **94**, 759–773 (2017).
63. Marsh, S. E. et al. Dissection of artifactual and confounding glial signatures by single-cell sequencing of mouse and human brain. *Nat. Neurosci.* **25**, 306–316 (2022).
64. Cardona, A. E., Huang, D., Sasse, M. E. & Ransohoff, R. M. Isolation of murine microglial cells for RNA analysis or flow cytometry. *Nat. Protoc.* **1**, 1947–1951 (2006).
65. Bennett, M. L. et al. New tools for studying microglia in the mouse and human CNS. *Proc. Natl Acad. Sci. USA* **113**, E1738–E1746 (2016).
66. Collins, H. Y. & Bohlen, C. J. Isolation and culture of rodent microglia to promote a dynamic ramified morphology in serum-free medium. *J. Vis. Exp.* (**133**), 57122 (2018).
67. Smith, T., Heger, A. & Sudbery, I. UMI-tools: modeling sequencing errors in Unique Molecular Identifiers to improve quantification accuracy. *Genome Res.* **27**, 491–499 (2017).
68. Dobin, A. et al. STAR: ultrafast universal RNA-seq aligner. *Bioinformatics* **29**, 15–21 (2013).
69. Liao, Y., Smyth, G. K. & Shi, W. featureCounts: an efficient general purpose program for assigning sequence reads to genomic features. *Bioinformatics* **30**, 923–930 (2014).
70. McCarthy, D. J., Campbell, K. R., Lun, A. T. L. & Wills, Q. F. Scater: pre-processing, quality control, normalization and visualization of single-cell RNA-seq data in R. *Bioinformatics* **33**, 1179–1186 (2017).
71. Van de Sande, B. et al. A scalable SCENIC workflow for single-cell gene regulatory network analysis. *Nat. Protoc.* **15**, 2247–2276 (2020).
72. Janky, R. et al. iRegulon: from a gene list to a gene regulatory network using large motif and track collections. *PLoS Comput. Biol.* **10**, e1003731 (2014).

Acknowledgements

Author contributions

R.L. and M.L. designed the experiments. R.L. and Y.Z. performed most of the experiments. T.Y. performed the experiments that involved cultured mouse microglia. R.W., T.Y., X.Zha., X.Zho. and L.Z. performed scRNA-seq and analysis. Z.W. and Y.L. developed the ATP fluorescent sensor, GRAB$_{ATP}$. H.L. performed the in vivo

imaging. Y.Z. and F.Z. packaged AAV viruses. R.L. and M.L. wrote the manuscript with contributions from all of the authors.

Additional information

Extended data are available for this paper at https://doi.org/10.1038/s41592-022-01547-7.

Supplementary information The online version contains supplementary material available at https://doi.org/10.1038/s41592-022-01547-7.

Correspondence and requests for materials should be addressed to Rui Lin or Minmin Luo.

Peer review information *Nature Methods* thanks Sandra Siegert, Amanda Sierra and the other, anonymous, reviewer(s) for their contribution to the peer review of this work. Primary Handling Editor: Nina Vogt, in collaboration with the *Nature Methods* team. Peer reviewer reports are available.

Reprints and permissions information is available at www.nature.com/reprints.
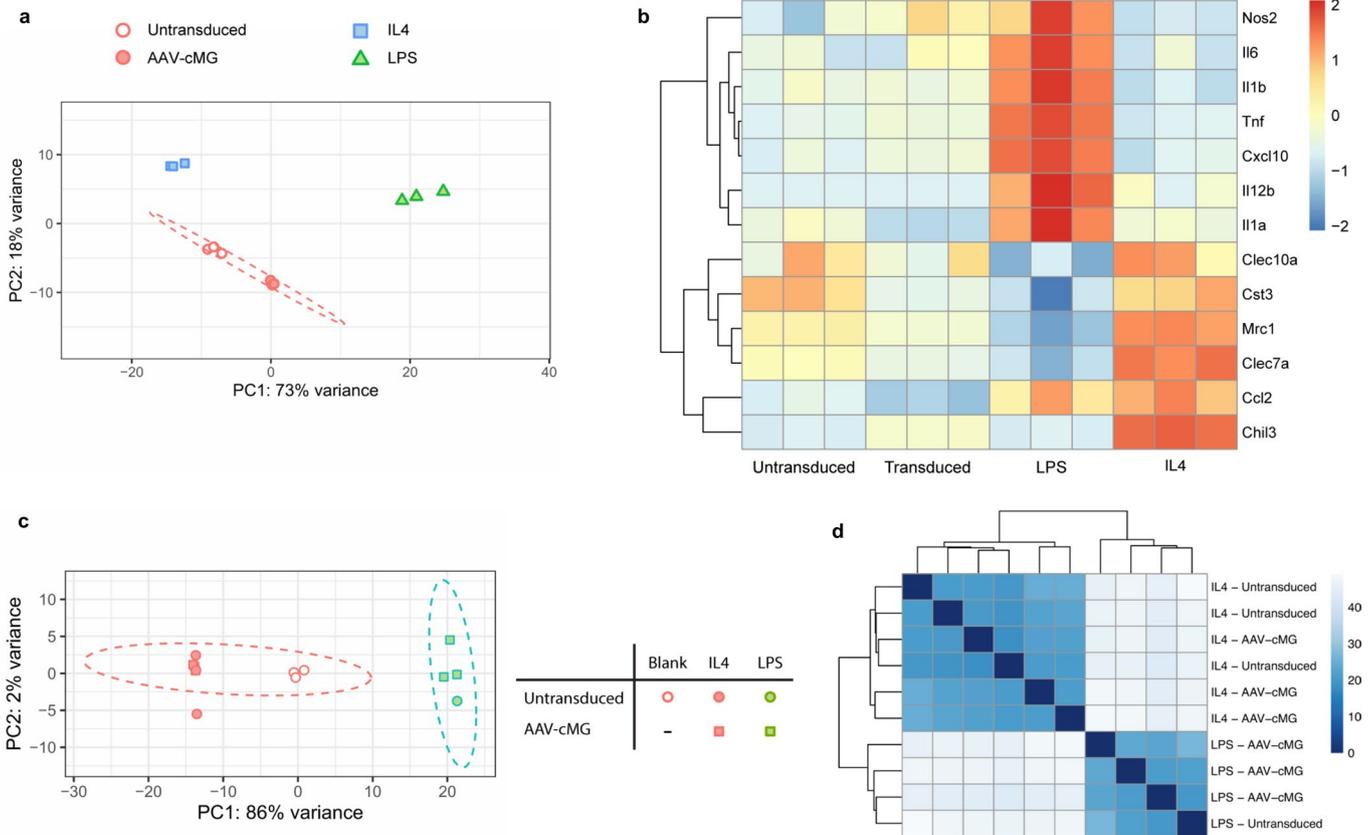
Extended Data Fig. 1 | AAV-cMG transduction does not activate microglia and does not blunt microglial responses to lipopolysaccharide (LPS) and interleukin-4 (IL4). a, Principal component analysis of the transcriptomes of cultured mouse microglia from four treatment groups: control untransduced, lipopolysaccharide (LPS)-treated, interleukin-4-treated (IL4) and AAV-cMG-transduced group ($n=3$ replicates for each group). **b**, Hierarchical clustering performed on marker genes of microglial states for different treatment groups as shown in (**a**). The color bar represents the z-score of the relative gene expression. **c**, Principal component analysis of the transcriptomes of cultured mouse microglia from five treatment groups: untransduced microglia ($n=3$), untransduced microglia treated with LPS ($n=1$), untransduced microglia treated with IL4 ($n=3$), AAV-cMG-transduced microglia treated with LPS ($n=3$), and AAV-cMG-transduced microglia treated with IL4 ($n=3$). **d**, Hierarchical clustering performed on LPS- or IL4-treated microglia as shown in (**c**). The color bar represents the Euclidean distance between samples.
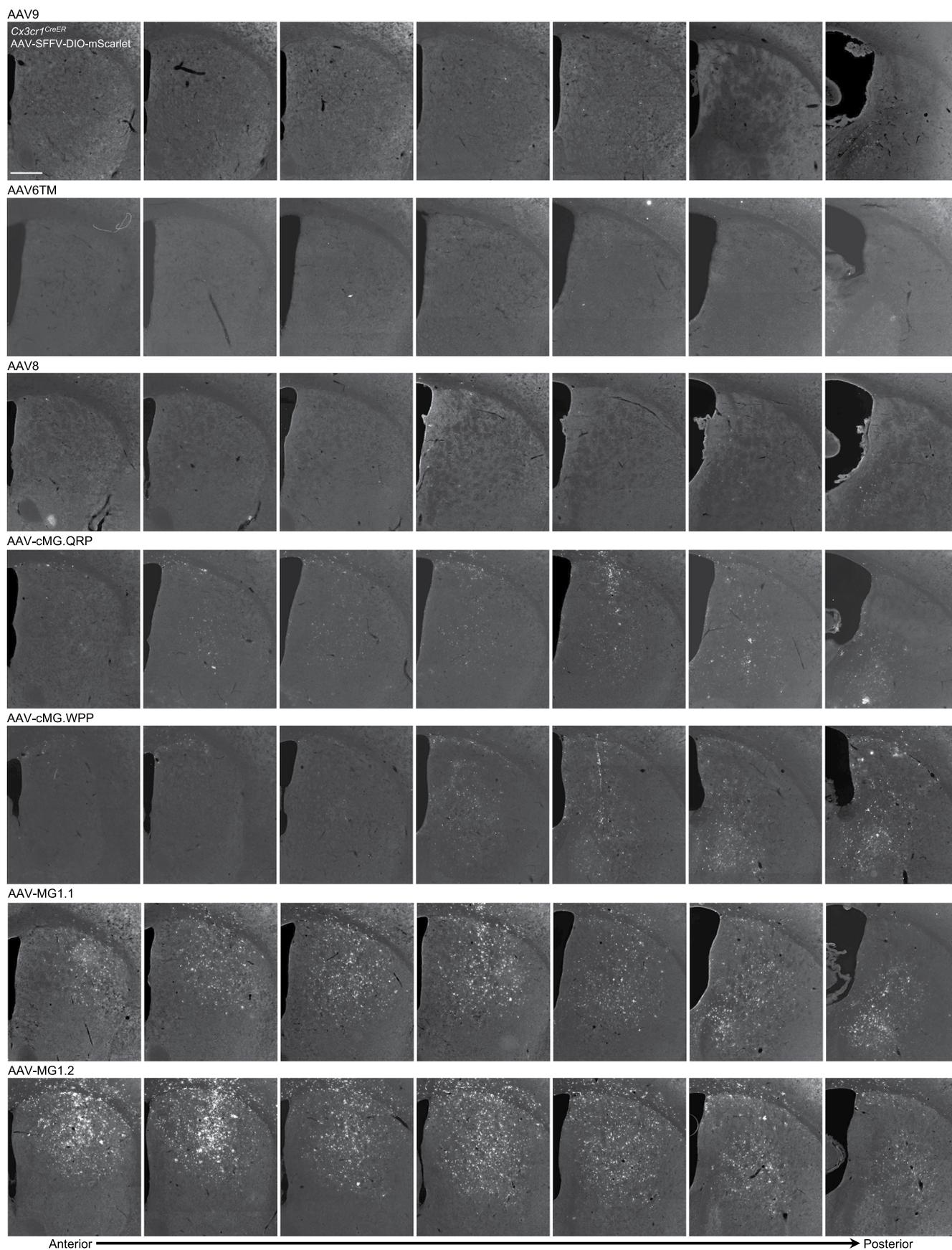
Extended Data Fig. 2 | Representative images of serial coronal sections of the striatum from *Cx3cr1^CreER* mice injected with AAV9-, AAV6TM-, AAV8-, AAV-cMG.QRP-, AAV-cMG.WPP-, AAV-MG1.1-, or AAV-MG1.2-SFFV-DIO-mScarlet. Scale bar, 500 μm.
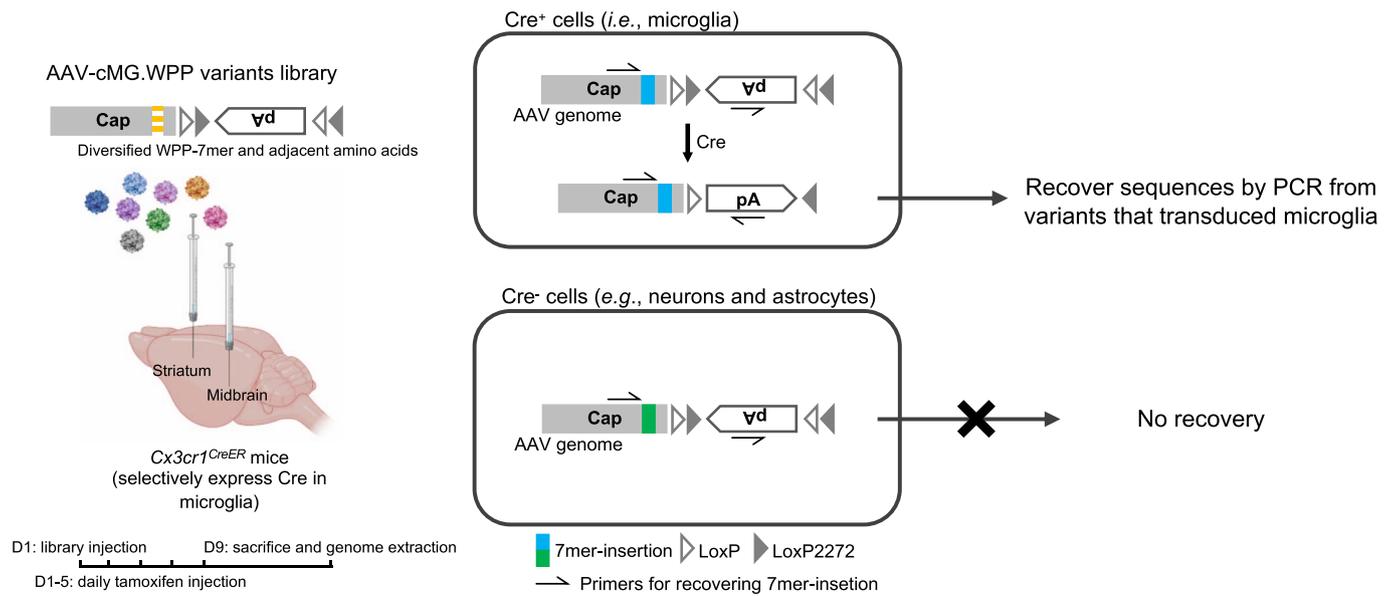
Extended Data Fig. 3 | Schematic of in vivo selection of AAV-cMG.WPP variants library by the Cre recombination-based AAV targeted evolution (CREATE) strategy. The AAV-cMG.WPP variants library was injected into the striatum and the midbrain of *Cx3cr1^CreER* mice, which selectively express Cre recombinase in microglia. For those variants that successfully transduced microglia, Cre flipped the double-floxed inverse open reading frame (DIO) on their AAV genomes, allowing the selective amplification and recovery of the heptamer insertion sequences using a pair of primers.
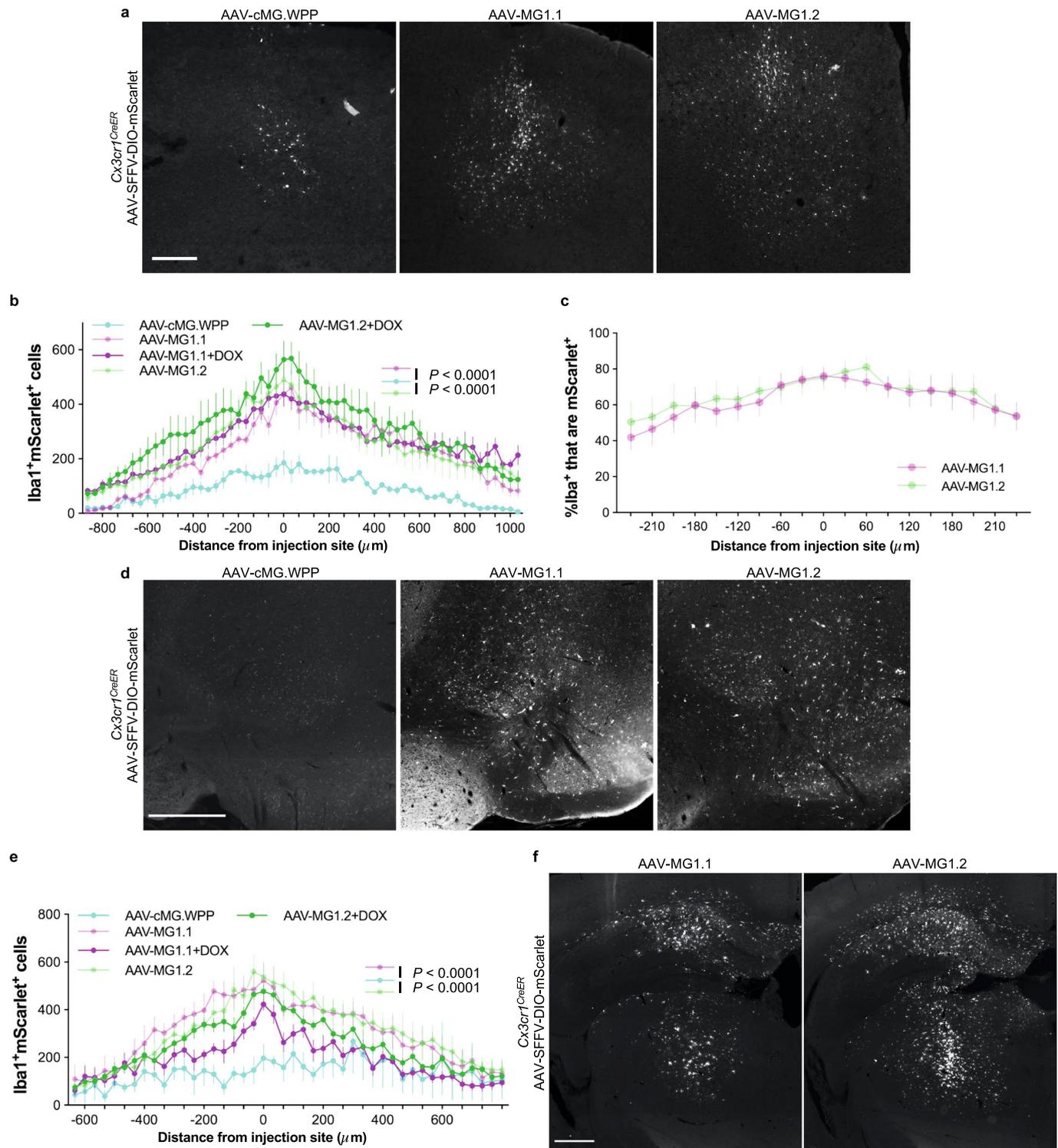
Extended Data Fig. 4 | AAV-MGs mediate efficient microglial transduction in vivo. a, Representative images showing the mScarlet expression patterns in the orbitofrontal cortex (OFC) of *Cx3cr1*[CreER] mice injected with AAV-cMG.WPP-, AAV-MG1.1-, or AAV-MG1.2-SFFV-DIO-mScarlet. Scale bar, 500 μm. **b**, Cell counts of mScarlet and Iba double-positive cells in the OFC of *Cx3cr1*[CreER] mice injected with AAV-cMG.WPP- (*n* = 3), AAV-MG1.1- (*n* = 5), or AAV-MG1.2-SFFV-DIO-mScarlet (*n* = 5) (two-way ANOVA with Tukey's post-hoc test; cMG.WPP vs. MG1.1: $P < 0.0001$; AAV-cMG.WPP vs. AAV-MG1.2: $P < 0.0001$). Data are presented as mean ± standard error of the mean (s.e.m.). **c**, Quantification of the percentage of Iba-positive microglia that are labeled by mScarlet in the OFC of *Cx3cr1*[CreER] mice injected with AAV-MG1.1- or AAV-MG1.2-SFFV-DIO-mScarlet (*n* = 5 mice for each group). The quantifications were conducted over an area of 1×1 mm². Data are presented as mean ± s.e.m. **d**, Representative images showing the mScarlet expression patterns in the midbrain of *Cx3cr1*[CreER] mice injected with AAV-cMG.WPP-, AAV-MG1.1-, or AAV-MG1.2-SFFV-DIO-mScarlet. Scale bar, 500 μm. **e**, Cell counts of mScarlet and Iba double-positive cells in the midbrain of *Cx3cr1*[CreER] mice injected with AAV-cMG.WPP- (*n* = 3), AAV-MG1.1- (*n* = 5), or AAV-MG1.2-SFFV-DIO-mScarlet (*n* = 5) (two-way ANOVA with Tukey's post-hoc test; cMG.WPP vs. MG1.1: $P < 0.0001$; AAV-cMG.WPP vs. AAV-MG1.2: $P < 0.0001$). Data are presented as mean ± s.e.m. **f**, Representative images showing the mScarlet expression patterns in the hippocampus and the thalamus of *Cx3cr1*[CreER] mice injected with AAV-MG1.1- or AAV-MG1.2-SFFV-DIO-mScarlet (right). Scale bar, 500 μm.
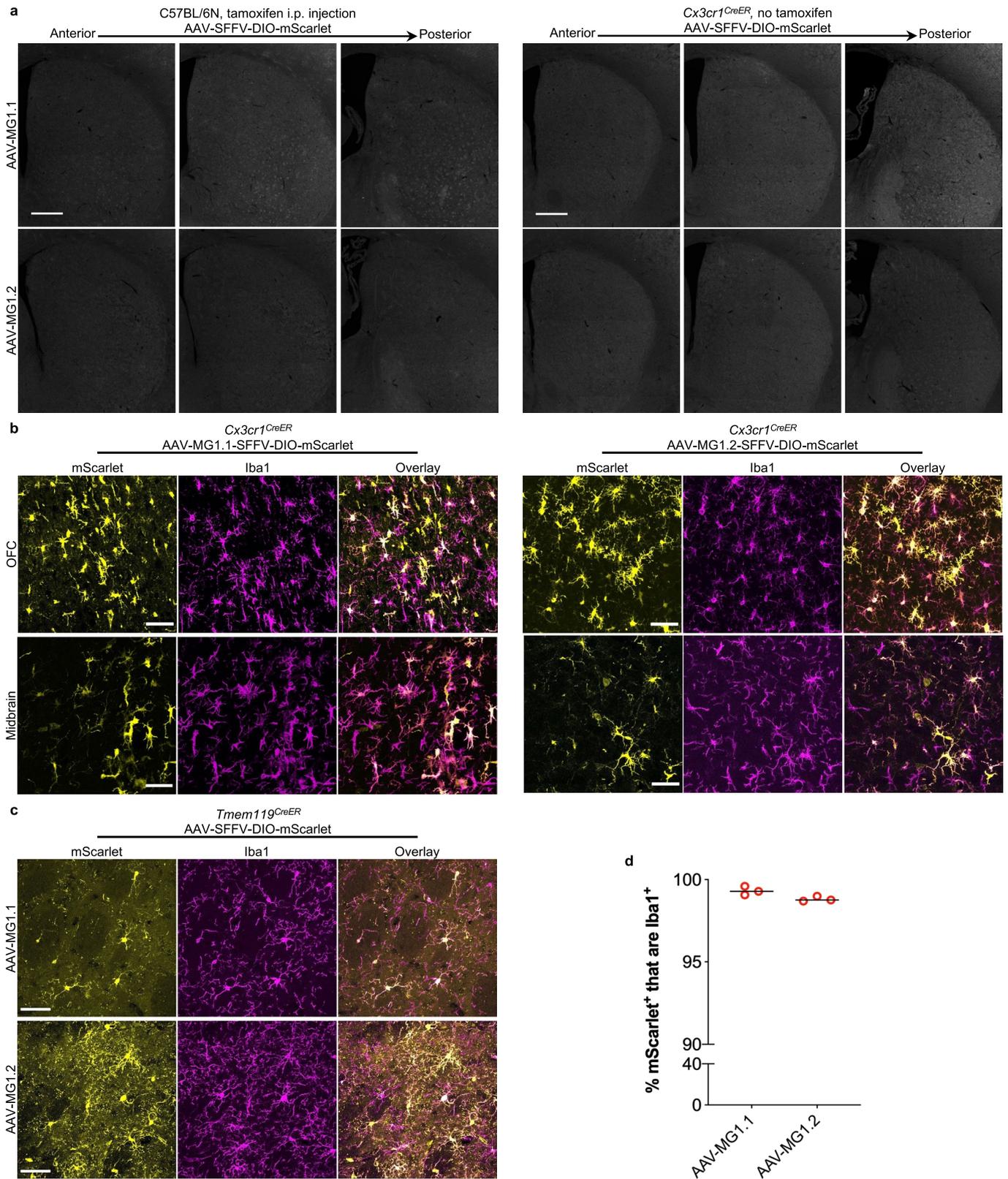
Extended Data Fig. 5 | See next page for caption.

Extended Data Fig. 5 | Selective Cre-dependent transgene expression in microglia by AAV-MGs. a, Representative images showing the striatum of mice injected with AAV-MG1.1- or AAV-MG1.2-SFFV-DIO-mScarlet. The left panel shows the striatum of C57BL/6N mice received intrastriatal virus injection together with i.p. tamoxifen injection. The right panel shows the striatum of $Cx3cr1^{CreER}$ mice received intrastriatal virus injection without tamoxifen administration. Scale bars, 500 μm. **b**, Representative images showing the colocalization of mScarlet and Iba$^+$ immunosignals in the OFC and the midbrain of $Cx3cr1^{CreER}$ mice injected with AAV-MG1.1- or AAV-MG1.2-SFFV-DIO-mScarlet. Scale bars, 50 μm. **c**, Representative images showing the colocalization of mScarlet and Iba$^+$ immunosignals in the striatum of $Tmem119^{CreER}$ mice injected with AAV-MG1.1- or AAV-MG1.2-SFFV-DIO-mScarlet. Scale bars, 50 μm. **d**, Quantification of the percentage of mScarlet and Iba double-positive cells among total mScarlet-positive cells in the striatum of $Tmem119^{CreER}$ mice injected with AAV-MG1.1- or AAV-MG1.2-SFFV-DIO-mScarlet. Data are presented as scatter and mean.
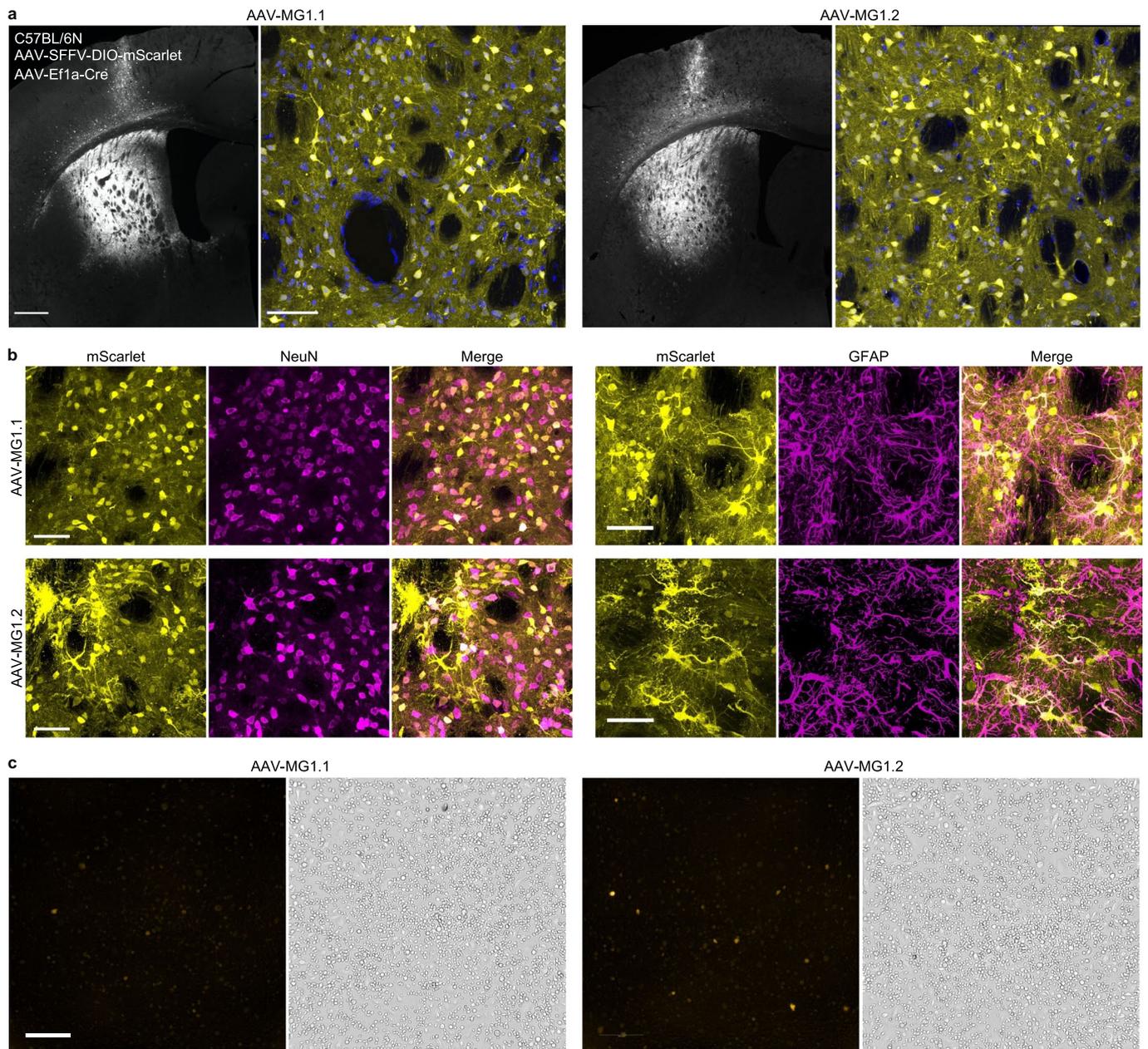
Extended Data Fig. 6 | AAV-MGs effectively transduce neurons and astrocytes in vivo but do not efficiently transduce cultured microglia. a, Representative images showing the mScarlet expression patterns in the striatum of C57BL/6 N mice injected with a virus mixture of AAV-Ef1a-Cre and AAV-MG1.1-SFFV-DIO-mScarlet or a virus mixture of AAV-Ef1a-Cre and AAV-MG1.2-SFFV-DIO-mScarlet. Yellow: mScarlet, blue: DAPI. Scale bars, 500 μm (slide scanning) and 100 μm (confocal images). **b**, Representative images showing the colocalization of mScarlet and NeuN[+]/GFAP[+] immunosignals in the striatum of C57BL/6 N mice injected with a virus mixture of AAV-Ef1a-Cre and AAV-MG1.1-SFFV-DIO-mScarlet or a virus mixture of AAV-Ef1a-Cre and AAV-MG1.2-SFFV-DIO-mScarlet. Scale bars, 50 μm. **c**, Representative fluorescent and bright-field images of cultured mouse microglia transduced with mScarlet reporter rAAVs packaged using AAV-MG1.1 or AAV-MG1.2. Scale bars, 200 μm.
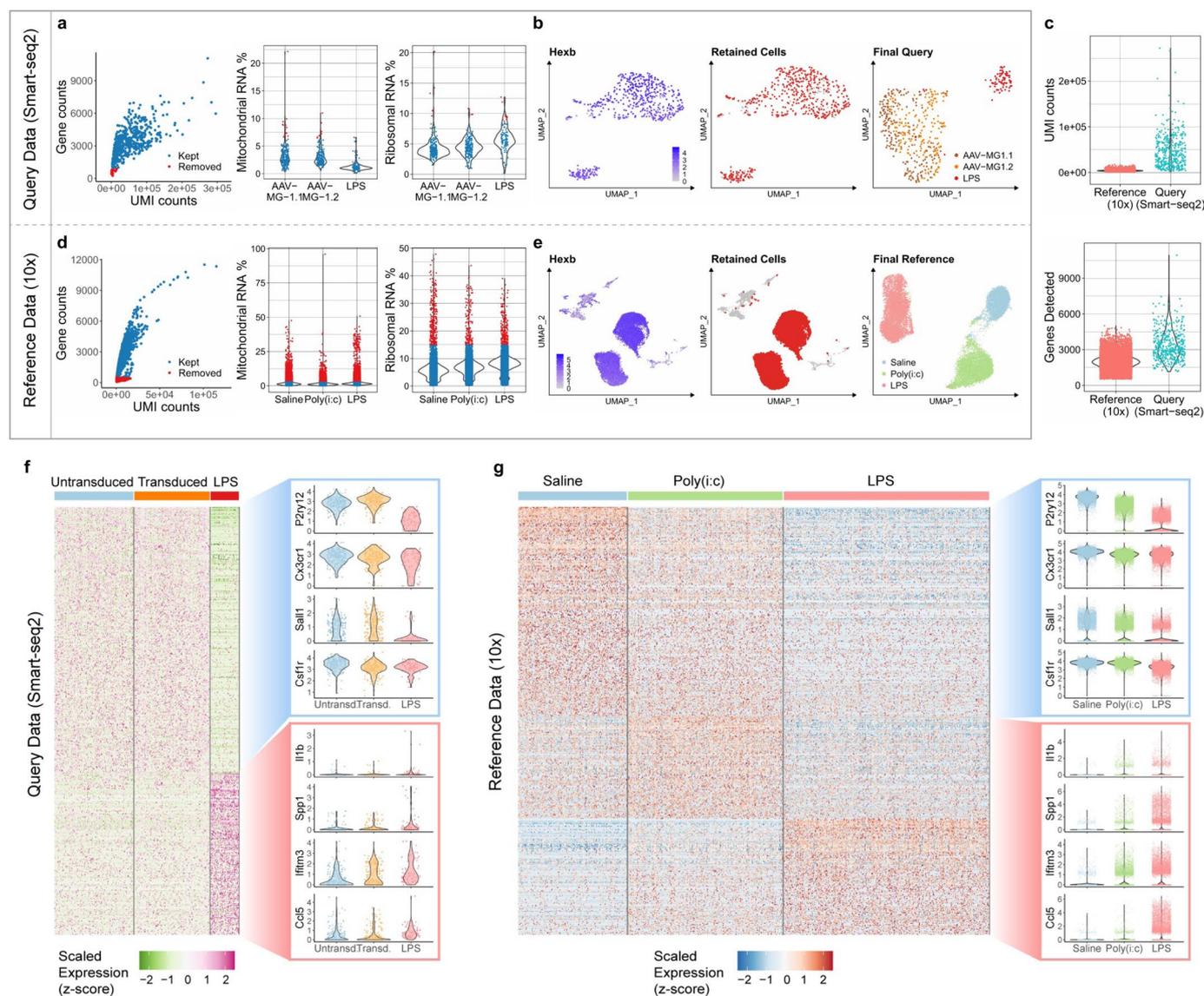
Extended Data Fig. 7 | Reference (10x) and query (Smart-seq2) single-cell RNA sequencing datasets characterizing the single-cell transcriptomes of microglia. a,d, Quantification of gene counts, UMI counts, the percentage of mitochondria RNA, and the percentage of ribosome RNA in the query (**a**) and the reference (**d**) datasets. Red dots represent sequenced microglia that failed to pass the quality check and were removed from subsequent analysis. **b,e,** UMAP plot of all cells (left and middle) and filtered microglia (right) sequenced using the Smart-seq2 protocol (**b**) or 10x Genomics platform (**e**). The blue color in the left panel indicates *Hexb* expression level. Cells with high *Hexb* expression (red in the middle panel) were identified as microglia and retained for subsequent analysis. **c,** Violin plots showing the UMI counts and the number of detected genes in the reference and the query datasets. **f,g,** Gene expression analysis of the query (**f**) and the reference (**g**) datasets. The heatmap shows the z-score of relative gene expression. The violin plots show the expression level of homeostatic marker genes (*P2ry12, Cx3cr1, Sall1* and *Csf1r*) and reactive marker genes (*Il1b, Spp1, Ifitm3* and *Ccl5*).
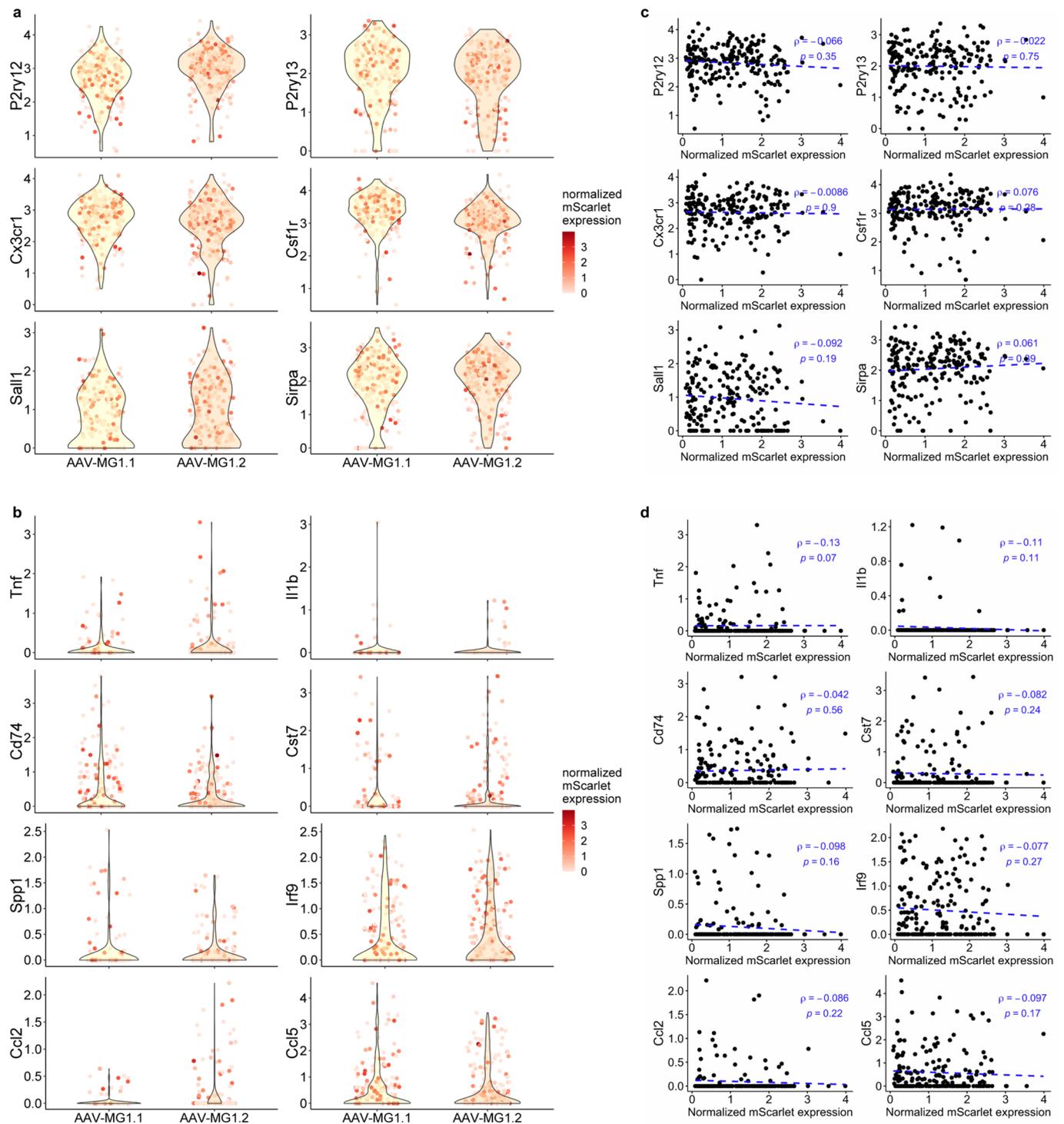
Extended Data Fig. 8 | The expression levels of homeostatic or reactive microglia marker genes are not correlated with AAV-MGs-mediated transgene expression. a,b, Violin plots showing the expression of classical homeostatic (**a**) and reactive (**b**) marker genes in the Smart-seq2-sequenced microglia from *Cx3cr1^CreER* mice injected with AAV-MG1.1- or AAV-MG-1.2-SFFV-DIO-mScarlet. Microglia that have no *mScarlet* transcript detected (normalized mScarlet expression = 0) are annotated as 'untransduced'. **c,d,** Scatter plots showing the expression levels of classical homeostatic (**c**) and reactive (**d**) marker genes against the expression levels of *mScarlet* in AAV-MGs-transduced microglia sequenced using Smart-seq2. The Spearman correlation coefficient and the significance level are shown in each panel.
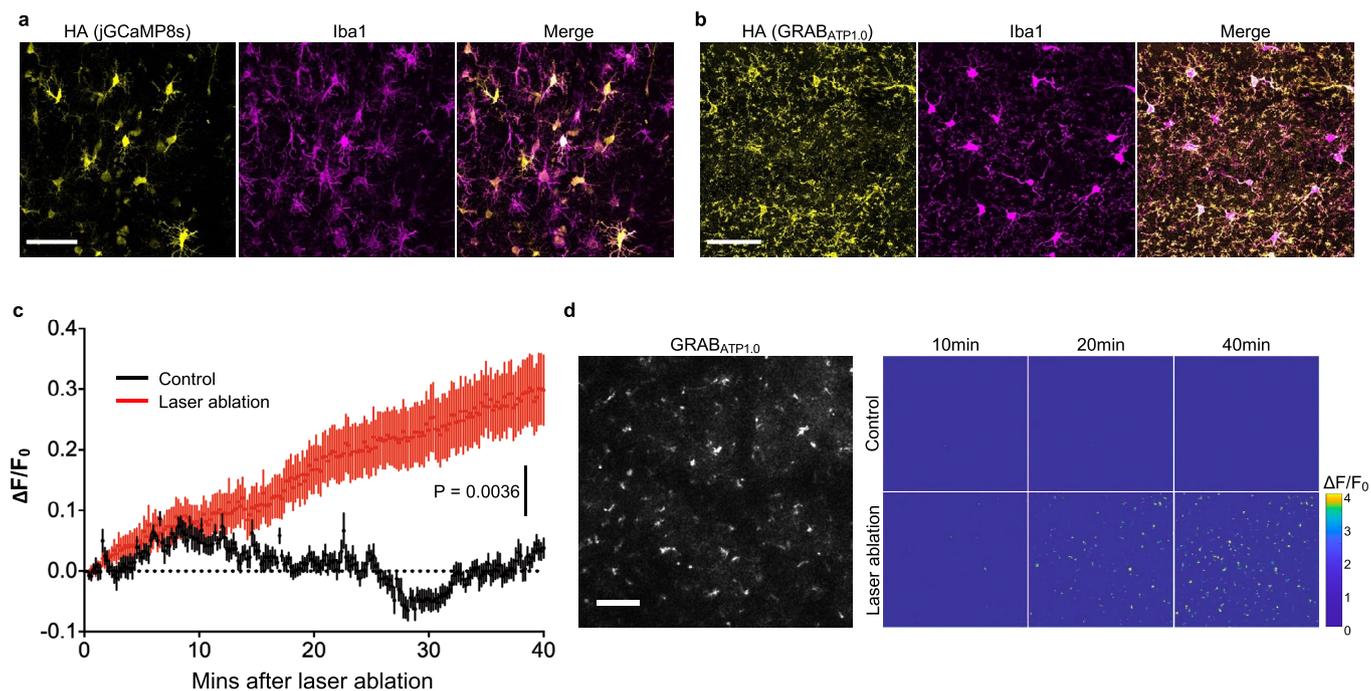
Extended Data Fig. 9 | AAV-MG1.2 enables in vivo two-photon imaging of microglia extracellular ATP changes following acute laser ablation. a, Representative images showing the colocalization of jGCaMP8s (HA-tag immunosignals) and Iba[+] immunosignals in the primary somatosensory (S1) cortex of *Cx3cr1^{CreER}* mice injected with AAV-MG1.2-SFFV-DIO-jGCaMP8s. Scale bar, 50 μm. **b**, Representative images showing the colocalization of GRAB$_{ATP1.0}$ (HA-tag immunosignals) and Iba[+] immunosignals in the S1 cortex of *Cx3cr1^{CreER}* mice injected with AAV-MG1.2-SFFV-DIO-GRAB$_{ATP1.0}$. Scale bar, 50 μm. **c**, Quantification of GRAB$_{ATP1.0}$ fluorescence signals at microglial somata in the control mice (*n* = 10 cells; black) or in the mice that received laser ablation (*n* = 16 cells; red) (two-way ANOVA; *P* values as listed in the figure). Data are presented as mean ± s.e.m. **d**, Image showing GRAB$_{ATP1.0}$ expression in microglia and heatmaps showing the GRAB$_{ATP1.0}$ fluorescence signals at 10, 20, and 40 min in the imaging session. For the laser ablation group, the laser was applied at the center of field of view at the beginning (0 min) of the imaging session. Scale bar, 100 μm.

A *Cx3CR1^CreER:Rosa26-LSL-Cas9-GFP*
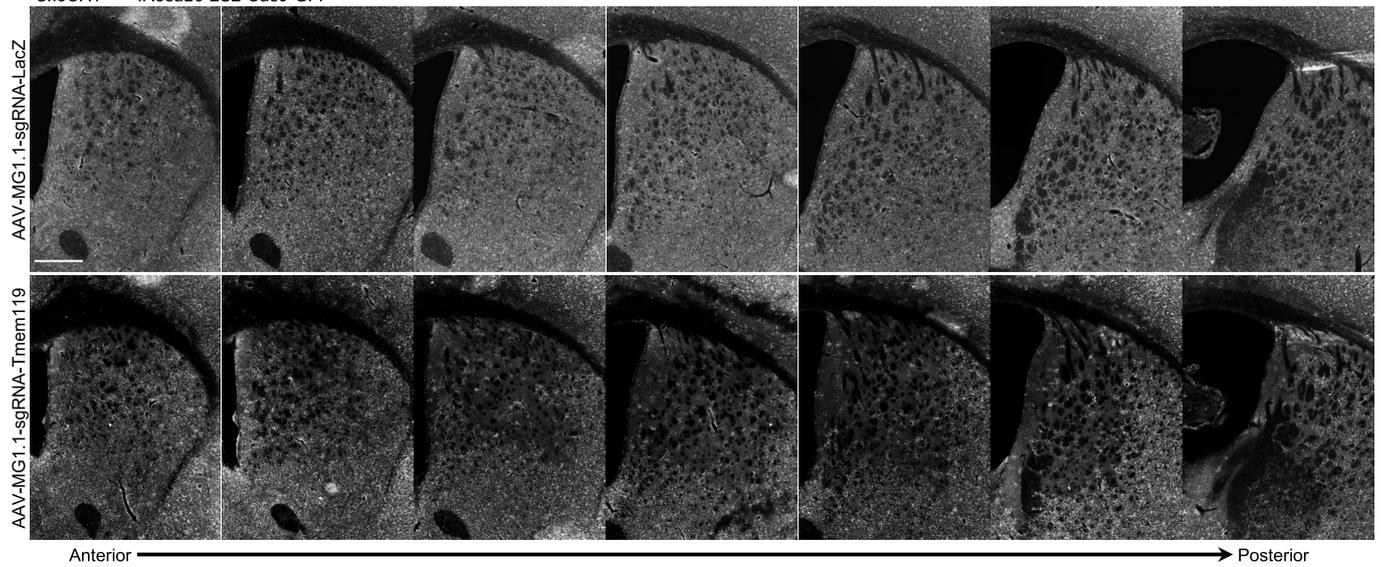
B *Cx3CR1^CreER:Rosa26-LSL-Cas9-GFP*

C

D
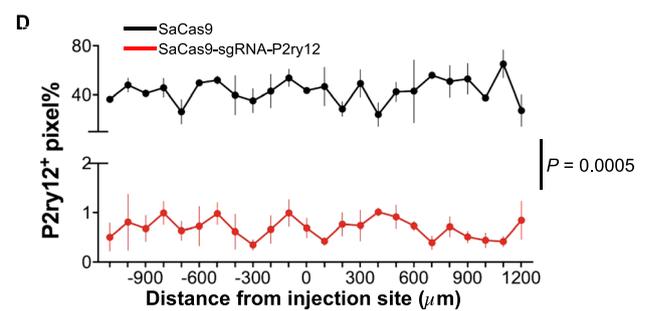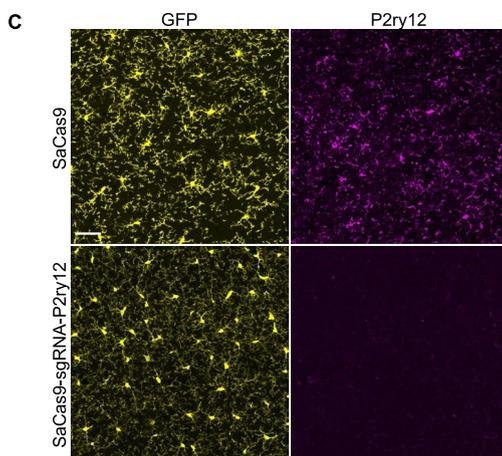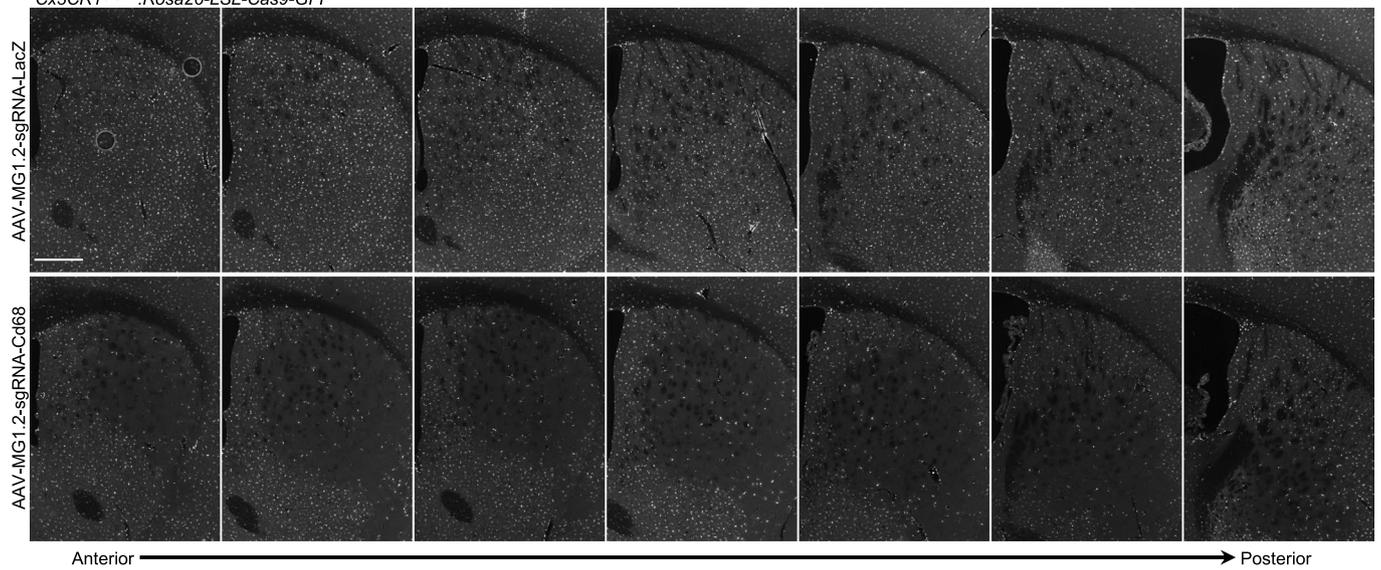
Extended Data Fig. 10 | See next page for caption.

Extended Data Fig. 10 | In vivo microglia-specific gene knockout mediated by AAV-MGs. a, Representative images of serial coronal sections of the striatum from a *Cx3cr1*[CreER]:*Rosa26-LSL-Cas9-GFP* mouse injected with AAV-MG1.1-sgRNA-LacZ or AAV-MG1.1-sgRNA-Tmem119. The brain sections were immunostained against Tmem119. Scale bar, 500 μm. **b**, Representative images of serial coronal sections of the striatum from a *Cx3cr1*[CreER]:*Rosa26-LSL-Cas9-GFP* mouse injected with AAV-MG1.2-sgRNA-LacZ or AAV-MG1.2-sgRNA-Cd68. The brain sections were immunostained against Cd68. Scale bar, 500 μm. **c**, Representative images of the S1 cortex of *Cx3cr1*[GFP] mice injected with AAV-MG1.2-CMV-SaCas9 or AAV-MG1.2-CMV-SaCas9-U6-sgRNA-P2ry12. The brain sections were immunostained against P2ry12. Scale bar, 100 μm. **d**, Quantification of the percentage of P2ry12-positive pixels in a 1×1 mm² region in the S1 cortex of *Cx3cr1*[GFP] mice injected with AAV-MG1.2-CMV-SaCas9 ($n=2$) or AAV-MG1.2-CMV-SaCas9-sgRNA-P2ry12 ($n=3$) (two-way ANOVA; *P* values as listed in the figure). Data are presented as mean ± s.e.m.

Reporting Summary

Nature Portfolio wishes to improve the reproducibility of the work that we publish. This form provides structure for consistency and transparency in reporting. For further information on Nature Portfolio policies, see our Editorial Policies and the Editorial Policy Checklist.

Statistics

For all statistical analyses, confirm that the following items are present in the figure legend, table legend, main text, or Methods section.

n/a	Confirmed	
☐	☒	The exact sample size (*n*) for each experimental group/condition, given as a discrete number and unit of measurement
☐	☒	A statement on whether measurements were taken from distinct samples or whether the same sample was measured repeatedly
☐	☒	The statistical test(s) used AND whether they are one- or two-sided *Only common tests should be described solely by name; describe more complex techniques in the Methods section.*
☒	☐	A description of all covariates tested
☐	☒	A description of any assumptions or corrections, such as tests of normality and adjustment for multiple comparisons
☐	☒	A full description of the statistical parameters including central tendency (e.g. means) or other basic estimates (e.g. regression coefficient) AND variation (e.g. standard deviation) or associated estimates of uncertainty (e.g. confidence intervals)
☐	☒	For null hypothesis testing, the test statistic (e.g. *F*, *t*, *r*) with confidence intervals, effect sizes, degrees of freedom and *P* value noted *Give P values as exact values whenever suitable.*
☒	☐	For Bayesian analysis, information on the choice of priors and Markov chain Monte Carlo settings
☒	☐	For hierarchical and complex designs, identification of the appropriate level for tests and full reporting of outcomes
☒	☐	Estimates of effect sizes (e.g. Cohen's *d*, Pearson's *r*), indicating how they were calculated

Our web collection on statistics for biologists contains articles on many of the points above.

Software and code

Policy information about availability of computer code

Data collection	Custom Python, Matlab, and R codes were used to generated NGS data. For confocal imaging, Zen (2.3) was used. For slide scanning, Olyvia was used.
Data analysis	Cell Ranger (10x genomics); Matlab (version R2018a); GraphPad Prism (9.02); ImageJ (FIJI) (version 2.1.0); STAR (v2.7.9a); UMI-tools (v1.1.2); Subread (v1.6.3); scater (v1.18.6); Seurat (v4.0.2); pySCENIC (v0.11.2); Cytoscape (v3.2.0); iRegulon (v 1.3); Imaris (v 9.8); R (R version 4.0.3); RStudio (1.4.1103); Microsoft Excel (16.59)

For manuscripts utilizing custom algorithms or software that are central to the research but not yet described in published literature, software must be made available to editors and reviewers. We strongly encourage code deposition in a community repository (e.g. GitHub). See the Nature Portfolio guidelines for submitting code & software for further information.

Data

Policy information about availability of data

All manuscripts must include a data availability statement. This statement should provide the following information, where applicable:
- Accession codes, unique identifiers, or web links for publicly available datasets
- A description of any restrictions on data availability
- For clinical datasets or third party data, please ensure that the statement adheres to our policy

All numerical source data are provided with this paper. The NGS datasets reported in this work are available under the GEO accession number GSE197743. The GRCm38 reference genome assembly was downloaded from https://nov2020.archive.ensembl.org/Mus_musculus/Info/Index. The following plasmids are deposited to Addgene: rAAV2/cMG (184539), rAAV2/MG1.1 (184540), rAAV2/MG1.2 (184541), rAAV2/cMG.WPP (184542), and rAAV2/cMG.QRP (184543). Other data and plasmids generated in this study are available from the corresponding authors upon reasonable request.

Field-specific reporting

Please select the one below that is the best fit for your research. If you are not sure, read the appropriate sections before making your selection.

☒ Life sciences   ☐ Behavioural & social sciences   ☐ Ecological, evolutionary & environmental sciences

For a reference copy of the document with all sections, see nature.com/documents/nr-reporting-summary-flat.pdf

Life sciences study design

All studies must disclose on these points even when the disclosure is negative.

Sample size	No hypothesis based experiment was performed. Therefore, the sample size was not pre-determined. It is a common practice to use 3-5 animals for each group for analyzing AAV efficiency (Rosario et al., Molecular Therapy - Methods & Clinical Development, 2016; Körbelin et al., Molecular Therapy, 2016; Koerber et al., Molecular Therapy, 2009; Tervo et al., Neuron, 2016; Hanlon Molecular Therapy - Methods & Clinical Development, 2019; Deverman et al., Nature Biotechnology, 2016). The sample sizes of our scRNA-seq datasets and in vivo imaging studies are comparable with previous studies (Li et al., Neuron, 2019; Hammond et al., Immunity, 2019; Haynes et al., Nature Neuroscience, 2006).
Data exclusions	No data were excluded.
Replication	All fluorescence intensity, transduction rate, cell counting, and immunostaining experiments were independently performed at least 3 times with similar results, except the Iba1 co-staining experiment performed in Tmem119CreER mice depicted in Extended Data Fig. 5c,d (1 experiment). The samples for single-cell RNA sequencing experiment were collected once. The cultured microglia RNA sequencing experiments were independently performed twice.
Randomization	Allocation of all samples, including mice and cultured cells, into different groups was random.
Blinding	Experimenters were not blinded to group allocation during data collection. Different groups of samples were collected and processed using the same protocols. Experimenters were not blinded during data analysis as all analysis were done by softwares or codes. So blinding would not be helpful in these experiments.

Reporting for specific materials, systems and methods

We require information from authors about some types of materials, experimental systems and methods used in many studies. Here, indicate whether each material, system or method listed is relevant to your study. If you are not sure if a list item applies to your research, read the appropriate section before selecting a response.

Materials & experimental systems

n/a	Involved in the study
☐	☒ Antibodies
☐	☒ Eukaryotic cell lines
☒	☐ Palaeontology and archaeology
☐	☒ Animals and other organisms
☒	☐ Human research participants
☒	☐ Clinical data
☒	☐ Dual use research of concern

Methods

n/a	Involved in the study
☒	☐ ChIP-seq
☒	☐ Flow cytometry
☒	☐ MRI-based neuroimaging

Antibodies

Antibodies used	anti-Iba1, 019-19741, Wako; anti-TMEM119, ab209064, Abcam; anti-CD68, ab53444, Abcam; anti-P2RY12, 848002, BioLegend; anti-HA, 1:500, 11867423001, Roche; Goat anti-rabbit-AF647, 111-605-144, Jackson ImmunoResearch; Goat anti-rabbit-AF488, 111-545-003, Jackson ImmunoResearch; Goat anti-rat-Cy5, 112-175-143, Jackson ImmunoResearch.
Validation	These antibodies were extensively used in previous studies. Staining pattern was compared to existing literature when possible. See the detailed lists of references below. 1. anti-Iba1, 019-19741, Wako: https://labchem-wako.fujifilm.com/us/product_data/docs/00055446_doc03.pdf 2. anti-TMEM119, ab209064, Abcam: https://www.abcam.com/tmem119-antibody-28-3-microglial-marker-ab209064.html 3. anti-CD68, ab53444, Abcam: https://www.abcam.com/cd68-antibody-fa-11-ab53444.html 4. anti-P2RY12, 848002, BioLegend: https://www.biolegend.com/fr-ch/products/purified-anti-p2ry12-antibody-14063 5. anti-HA, 1:500, 11867423001, Roche: https://www.sigmaaldrich.cn/CN/en/search/roahaha?focus=papers&page=1&perpage=30&sort=relevance&term=roahaha&type=citation_search

Eukaryotic cell lines

Policy information about cell lines

Cell line source(s)	HEK293T (ATCC CRL-3216) used for AAV packaging is obtained from ATCC.
Authentication	Not performed
Mycoplasma contamination	Not tested
Commonly misidentified lines (See ICLAC register)	Not used

Animals and other organisms

Policy information about studies involving animals; ARRIVE guidelines recommended for reporting animal research

Laboratory animals	Cx3cr1CreER mice (021160, Cx3cr1tm2.1(cre/ERT2)Litt/WganJ), Cx3cr1GFP mice (005582, Cx3cr1tm1Litt/J), Tmem119CreER mice (031820, Tmem119em1(cre/ERT2)Gfng/J), and Rosa26-LSL-Cas9-GFP mice (024857, Gt(ROSA)26Sortm1(CAG-cas9*,-EGFP)Fezh/J) mice were obtained from Jackson Laboratory. Adult mice (10-16 weeks) of either sex were used for in vivo virus injection. The postnatal day 1 (P1) and adult C57BL/6N wildtype mice (8-10 weeks) were obtained from Beijing Vital River Laboratory Animal Technology. Mice were maintained with a 12/12 hour photoperiod (light on at 8AM) and were provided food and water ad libitum. Ambient temperature was kept at 25 °C with humidity at 50%.
Wild animals	This study did not involve wild animals.
Field-collected samples	This study did not involve samples collected from the fields.
Ethics oversight	Animal care and use followed the approval of the Animal Care and Use Committee of the National Institute of Biological Sciences, Beijing in accordance with the Regulations for the Administration of Affairs Concerning Experimental Animals of China.

Note that full information on the approval of the study protocol must also be provided in the manuscript.